

# SPATIALLY ADAPTED FIRST AND SECOND ORDER REGULARIZATION FOR IMAGE RECONSTRUCTION: FROM AN IMAGE SURFACE PERSPECTIVE

QIUXIANG ZHONG\*, RYAN WEN LIU†, AND YUPING DUAN‡

**Abstract.** It is well-known that images are comprised of multiple objects at different scales. Thus, we propose a spatially adapted first and second order regularization for image reconstruction to better localize image features. More specifically, we minimize the  $L^1$  norm of the *Weingarten map* of the image surface  $(x, f(x))$  for a given image  $f : \Omega \rightarrow \mathbb{R}$ , which is further reformulated into a combined first and second order regularizer with adapted parameters. We analytically prove our model can keep the greyscale intensity contrasts of images and preserve edges. In what follows, we present the numerical solution to the proposed model by employing the alternating direction method of multipliers (ADMM) and analyze the convergence under certain conditions. Various numerical experiments on image denoising, deblurring and inpainting are implemented to demonstrate the effectiveness and efficiency of the proposed regularization scheme. By comparing with several state-of-the-art methods on synthetic and real image reconstruction problems, it is shown that the proposal can enhance image regions containing fine details and smoothness in homogeneous regions, while being simple and efficiently numerically solvable.

**Key words.** Image reconstruction, image surface, Weingarten map, spatially adaptive regularization, contrast-preserving

**AMS subject classifications.**

**1. Introduction.** Image restoration has attracted extensive attention in the fields of image processing and computer vision, where variational formulations are particularly effective in high quality recovery. Let  $\Omega$  be an open bounded subset of  $\mathbb{R}^n$  with Lipschitz continuous boundary,  $f : \Omega \rightarrow \mathbb{R}$  be a given image defined on the domain  $\Omega$ , and  $u : \Omega \rightarrow \mathbb{R}$  be the latent clean image. Rudin, Osher and Fatemi [41] proposed the total variation (TV) regularization for image restoration as a constrained minimization problem (ROF model)

$$(1.1) \quad \min_u \int_{\Omega} |\nabla u| dx, \quad \text{with} \quad \int_{\Omega} u dx = \int_{\Omega} f dx \quad \text{and} \quad \int_{\Omega} (u - f)^2 = \sigma^2,$$

where the constraints correspond to the assumption that the noise is of zero mean and standard deviation  $\sigma$ . Chambolle and Lions [10] linked the constrained minimization problem (1.1) and the following minimization problem

$$(1.2) \quad \min_u \int_{\Omega} |\nabla u| dx + \frac{1}{2\lambda} \int_{\Omega} (u - f)^2 dx,$$

where  $\lambda \equiv \text{const} > 0$  represents the Lagrange multiplier associated with the constraints. Indeed, an alternative way to express the TV model (1.2) for image reconstruction is given as

$$(1.3) \quad \min_u \alpha \int_{\Omega} |\nabla u| dx + \frac{1}{2} \int_{\Omega} (u - f)^2 dx,$$

---

\*Center for Applied Mathematics, Tianjin University, Tianjin, 300072, China, E-mail: zhongqiuxiang@tju.edu.cn

†School of Navigation, Wuhan University of Technology, Wuhan, Hubei, 430070, China, E-mail: wenliu@whut.edu.cn

‡Corresponding author. Center for Applied Mathematics, Tianjin University, Tianjin, 300072, China, E-mail: yuping.duan@tju.edu.cn

where  $\alpha = \lambda > 0$  is the regularization parameter. It is well-known that the Lagrange multiplier  $\lambda$  in (1.2) and the regularization parameter  $\alpha$  in (1.3) are used to control the trade-off between the data fidelity and regularization. The proper choice of  $\lambda$  and  $\alpha$  is delicate, and automatic methods have been developed in the literature. For example, Liao *et al.* [32] exploited the generalized cross-validation (GCV) technique to determine the regularization parameter used in each restoration step. Wen and Chan [47] used the Morozov’s discrepancy principle to find the best regularization parameter. Recently, parameter learning has been investigated in a bilevel optimization framework. Kunisch and Pock [28] casted the parameter selection as a learning problem by minimizing a certain loss function on a training data base. Reyes and Schönlieb [16] proposed a nonsmooth PDE constrained optimization approach to determine the correct noise model in TV image denoising.

Since images are comprised of multiple objects at different scales, it is more reasonable to use spatially varying variables instead of constant values. Possible small  $\lambda$  or  $\alpha$  is better in preserving the fine details in the images, while large  $\lambda$  or  $\alpha$  is good at achieving the smoothness in the homogeneous regions. Bertalmío *et al.* [5] proposed a variant TV restoration model using a set of  $\{\lambda_i\}_{i=1}^r$  with each one corresponding to a region set  $\{\Omega_i\}_{i=1}^r$  of the image, where  $\{\Omega_i\}_{i=1}^r$  can be obtained by simple segmentation algorithms. Almansa *et al.* [1] further developed the idea in [5] by using local variance estimation for obtaining  $\lambda(x) : \Omega \rightarrow \mathbb{R}$  without involving the segmentation in the process. Gilboa *et al.* [23] designed a pyramidal structure-texture decomposition of images, which isolated the noise and then estimated the spatially varying constraints based on local variance measures. Li *et al.* [31] extended this approach to Aubert-Aujol (AA) model for multiplicative noise removal. Dong *et al.* [18] improved the local variance estimator for  $\lambda(x)$  and update it automatically in a multi-scale TV scheme for removing Gaussian-distributed noise. The spatially adaptive regularization parameters was extended into the multi-scale vectorial  $L^\tau$ -TV framework [19] for color image restoration, which recover more texture details than classical color image restoration method [48]. Chung *et al.* [15] used a bilevel optimization approach in function space for the choice of spatially dependent regularization parameter for (1.2). In the case of impulsive noise, Hintermüller and Rincon-Camacho [27] proposed to develop the TVL1 model with spatially adapted regularization parameters based on local expected absolute value estimation for enhancing the image details and preserving the image edge. Another branch of these methods pursues a spatially varying  $\alpha(x) : \Omega \rightarrow \mathbb{R}$  for (1.3), which are also known as weighted TV. Strong and Chan [43] considered  $\alpha(x)$  as a spatially adapted weight in TV regularization to remove smaller-scaled noise while leaving larger-scaled features essentially intact. Yuan *et al.* [51] proposed a spatially weighted TV model in multiframe super-resolution reconstruction for efficiently reducing the staircase artifacts and preserving the edge information. Liu *et al.* [34] presented an adaptive-weighted TV minimization algorithm for sparse-view low-dose CT image reconstruction, where the corresponding weights can be adaptively adjusted by the local image-intensity gradient for preserving the edge details. Langer [29] realized the automated parameter selection of (1.3) based on the discrepancy principal. Recently, Hintermüller *et al.* [25, 26] computed the spatially adaptive weights for (1.3) using a bilevel optimization approach.

Although spatially varying  $\lambda(x)$  or  $\alpha(x)$  in the ROF model (1.2) and (1.3) can improve the reconstruction quality, they can not eliminate the staircase effect in the relatively large piecewise linear regions. Thus, high order variational models are proposed and studied in last two decades. Chambolle and Lions [10] proposed a high

order model by minimizing the infimal convolution of the total variation (ICTV) and the total variation of the image gradient. Assume a noisy image can be approximated by a piecewise constant part  $u_1$ , a piecewise smooth part  $u_2$  and noises, i.e.,  $f = u_1 + u_2 + n$ , the ICTV model is defined as

$$(1.4) \quad \min_{u_1, u_2} \alpha \int_{\Omega} |\nabla u_1| dx + \beta \int_{\Omega} |\nabla^2 u_2| dx + \frac{1}{2} \int_{\Omega} (u_1 + u_2 - f)^2 dx,$$

where  $\nabla^2 u_2$  denotes the Hessian of  $u_2$ . Later, Chan *et al.* [11] modified the ROF model by adding a nonlinear fourth order diffusion term to the associated Euler-Lagrange equation. Lysaker *et al.* [35, 36] proposed the noise removal model using the high order regularization term, that is

$$(1.5) \quad \min_u \int_{\Omega} |\nabla^2 u| dx + \frac{1}{2\lambda} \int_{\Omega} (u - f)^2 dx$$

with  $|\nabla^2 u| = \sqrt{|u_{xx}|^2 + |u_{xy}|^2 + |u_{yx}|^2 + |u_{yy}|^2}$ . The optimality condition of (1.5) gives a fourth-order partial differential equation, which have been further studied both theoretically and numerically in [24, 12, 49, 38]. Especially, Papafitsoros and Schönlieb [38] suggested the following combined first and second order variational model

$$(1.6) \quad \min_u \alpha \int_{\Omega} |\nabla u| dx + \beta \int_{\Omega} |\nabla^2 u| dx + \frac{1}{2} \int_{\Omega} (u - f)^2 dx,$$

which can recover both high detailed and homogeneous areas in the image with properly selected parameters  $\alpha > 0$  and  $\beta > 0$ . Recently, Reyes *et al.* [40] used a bilevel optimization approach for parameter learning in ICTV and TGV reconstruction models, where the  $\alpha$  and  $\beta$  are scalars learned from the training dataset.

Another important high order TV model was proposed by Bredies *et al.* [8], the so-called total generalized variation (TGV), which can integrate to incorporate smoothness from the first up to the  $k$ -th derivatives. The automatic regularization parameter selection proposed in [18] was applied to the TGV-regularized variational model [7]. In addition, curvature based regularization has also been introduced into image and surface reconstruction. The well-known Euler's elastica model [42, 44, 50] has achieved great success in image reconstruction problems, which minimizes the total elastica of all level contours in images

$$(1.7) \quad \min_u \int_{\Omega} \left( a + b \left( \nabla \cdot \frac{\nabla u}{|\nabla u|} \right)^2 \right) |\nabla u| dx + \frac{1}{2\lambda} \int_{\Omega} (u - f)^2 dx.$$

To the best of our knowledge, one has not identified, yet, the proper functional framework to formulate problem (1.7); see [17] for more discussion. By considering the associated *image surface* or *graph* of  $f$  in  $\mathbb{R}^{n+1}$ , the noise removal problem becomes the task of finding an approximate piecewise smooth surface. Then it is straightforward to employ the geometric invariants as the regularization such as Gaussian curvature [30, 20] and mean curvature [52, 53].

In this work, we propose a novel regularizer for image reconstruction, which is derived from the *Weingarten map* in differential geometry. Specifically, we minimize the following spatially adapted first and second order regularized energy functional

$$(1.8) \quad \min_u \int_{\Omega} \alpha(u) |\nabla u| dx + \int_{\Omega} \beta(u) |\nabla^2 u| dx + \frac{1}{2\lambda} \int_{\Omega} (u - f)^2 dx,$$



FIG. 1. Reconstructed results of “lena” by [38] and our proposed method. From left to right: (a) Gaussian noisy image,  $\sigma = 20$ , (b) the method in [38],  $PSNR=28.14$ ,  $SSIM=0.8083$ , (c) our proposed method,  $PSNR=29.25$ ,  $SSIM=0.8304$ , (d)  $\alpha(u)$  in our proposed method, (e)  $\beta(u)$  in our proposed method, respectively.

where  $\alpha(u)$  and  $\beta(u)$  are functions of  $u$  defined as

$$\alpha(u) = \left| \nabla \frac{1}{\sqrt{1 + |\nabla u|^2}} \right|, \quad \text{and} \quad \beta(u) = \frac{1}{\sqrt{1 + |\nabla u|^2}}.$$

We theoretically prove the proposed model (1.8) can preserve image contrasts, while neither the ROF model (1.2) nor the combined first and second order variational model (1.6) can. Due to the nonlinearity of  $\alpha(u)$  and  $\beta(u)$ , we use a dynamical update strategy to estimate them explicitly using the latest value of  $u$ . Then, an efficient numerical algorithm can be developed based on the proximal ADMM and the convergence of the algorithm is also discussed under certain conditions. Although the proposed model is not totally parameter-free, the selection of  $\lambda$  is relatively easy to handle according to the noise levels. Fig. 1 presents the recovered results obtained by the combined first and second-order model (1.6) and the proposed model (1.8), which demonstrates that more details are persevered by the spatially varying regularization term. Especially,  $\alpha(u)$  is large (relatively to  $\beta(u)$ ) nearby edges and texture structures to promote the first order regularizer, which together with the non-loss of contrast property makes the edges more enhanced. On the other hand,  $\beta(u)$  becomes large (relatively to  $\alpha(u)$ ) in homogenous regions to promote more the second order regularizer for overcoming staircase effect and enhancing the smoothness.

The rest of the paper is organized as follows. In Section 2, we introduce the Weingarten map-based regularization, its geometric properties, and derive the spatially adapted first and second regularization model for image reconstruction. Section 3 presents an proximal ADMM-based algorithm for solving the proposed model and discusses the convergence of the proposed algorithm. Section 4 implements the comprehensive numerical experiments to demonstrate its effectiveness and superiority. We summarize our specific work with a conclusion in Section 5.

Note that various derivation in the following sections may somehow lack rigorous mathematical foundations. Similar to the curvature-based regularizers such as Euler’s elastica and mean curvature, we do not know the proper functional space to formulate problem (1.8), obviously a subspace of  $L^2(\Omega)$ . Hence, the existence of minimizers will be tasks for further studies.

## 2. Weingarten map-based variational model.

**2.1. Description of our regularizer.** We regard the 2-dimensional image  $f$  defined on an open bounded subset  $\Omega \subset \mathbb{R}^2$  with the Lipschitz continuous boundary as the image surface  $(x, f(x))$  in  $\mathbb{R}^3$  with  $x \in \Omega$ . Consider the level set function

$\phi(x, z) = z - u(x)$ , the zero level set of which corresponds to the image surface  $\mathcal{S} = (x, u(x))$ . The unit normal for points on the zero level set  $\{(x, z) : \phi(x, z) = 0\}$  is defined as (cf. equation (1.2) in [37])

$$(2.1) \quad N_u = \frac{\nabla\phi}{|\nabla\phi|} = \frac{(\nabla u, -1)}{\sqrt{1 + |\nabla u|^2}}.$$

The established mean curvature regularized image denoising model in [52] is to minimize the divergence of the unit normal

$$(2.2) \quad \min_u \int_{\Omega} \left| \nabla \cdot \frac{\nabla u}{\sqrt{1 + |\nabla u|^2}} \right| dx.$$

The mean curvature regularization has been shown with good geometric properties including preserving contrast, edges and corners. Indeed, by minimizing the  $L^1$  norm of the first component of unit normal vector, we can obtain the following nonlinear first order regularizer

$$(2.3) \quad \min_u \int_{\Omega} \left| \frac{\nabla u}{\sqrt{1 + |\nabla u|^2}} \right| dx,$$

the denominator of which measures the surface area. Targeted to derive a combined first and second order regularization, we further pursue the gradient of the regularizer (2.3) and obtain

$$(2.4) \quad W_u = \nabla \left( \frac{\nabla u}{\sqrt{1 + |\nabla u|^2}} \right) = \nabla \frac{1}{\sqrt{1 + |\nabla u|^2}} \cdot \nabla u + \frac{1}{\sqrt{1 + |\nabla u|^2}} \nabla^2 u,$$

where  $\cdot$  denotes the dot product operation. It is easy to validate the matrix form of (2.4) can be expressed as

$$\begin{bmatrix} \frac{(1+u_y^2)u_{xx} - u_x u_y u_{xy}}{(1+u_x^2+u_y^2)^{3/2}} & \frac{(1+u_x^2)u_{xy} - u_x u_y u_{xx}}{(1+u_x^2+u_y^2)^{3/2}} \\ \frac{(1+u_y^2)u_{xy} - u_x u_y u_{yy}}{(1+u_x^2+u_y^2)^{3/2}} & \frac{(1+u_x^2)u_{yy} - u_x u_y u_{xy}}{(1+u_x^2+u_y^2)^{3/2}} \end{bmatrix},$$

which is the well-known *Weingarten map* or *shape operator* [45] and can be formally defined for each point  $p = (x, u(x)) \in \mathcal{S} \subset \mathbb{R}^3$  as a linear self-conjugate map

$$W_p := T_p \mathcal{S} \rightarrow T_p \mathcal{S}$$

with  $T_p \mathcal{S}$  denoting the tangent space of  $p$ . Particularly, the Weingarten map has very good geometric properties, which can be also interpolated as the combination of the *first fundamental form* I and the *second fundamental form* II of the image surface, i.e.,  $W_p = I^{-1}II$ . According to the differential geometry theory, the eigenvalues of  $W_p$  are the two principle curvatures  $\kappa_1, \kappa_2$  and it follows that

**Definition 2.1.** *Let  $\mathcal{S} \subset \mathbb{R}^3$  be an oriented surface and  $W_p$  be its Weingarten map at a point  $p = (x, u(x)) \in \mathcal{S}$ . Then the mean curvature and Gaussian curvature of  $\mathcal{S}$  can be defined by*

$$H_p := \frac{1}{2}(\kappa_1 + \kappa_2) = \frac{1}{2}\text{trace}(W_p),$$

$$G_p := \kappa_1 \kappa_2 = \det(W_p).$$

The Gaussian curvature is an intrinsic measure of the curvature, depending only on distances that measured on the surface, not on the way it is isometrically embedded in Euclidean space. Although the mean curvature is not intrinsic, a surface with zero mean curvature at all points is called the minimal surface. Instead of employing Gaussian curvature or mean curvature as the regularizer, we minimize the  $L^1$  norm of the Weingarten map and obtain the following regularization

$$(2.5) \quad \min_u \int_{\Omega} \left| \nabla \frac{1}{\sqrt{1+|\nabla u|^2}} \cdot \nabla u + \frac{1}{\sqrt{1+|\nabla u|^2}} \nabla^2 u \right| dx.$$

Similar to mean curvature regularizer, we illustrate that our regularizer (2.5) can preserve image contrasts. Consider a simple image  $f = h_{\chi_{B(0,R)}}(x,y)$  defined on a rectangle  $\Omega = (-2R, 2R) \times (-2R, 2R)$ , with  $\chi$  being the characteristic function,  $B(0,R)$  being an open disk in  $\mathbb{R}^2$  centered at the origin with radius  $R$ , and  $h > 0$ . As the image  $f$  is not even continuous, we generate a sequence of smooth radial symmetric functions  $\{u_n\}$ , which are pointwise converges to  $f$ . Then we can define  $\int_{\Omega} |W_f| dx dy$  to be  $\lim_{n \rightarrow +\infty} \int_{\Omega} |W_{u_n}| dx dy$ . More details of the setting can refer to [52].

**Lemma 2.2.** *Assume  $f = h_{\chi_{B(0,R)}}(x,y)$  is an image defined on a rectangle  $\Omega = (-2R, 2R) \times (-2R, 2R)$ , where  $\chi$  represents the characteristic function,  $B(0,R)$  denotes an open disk in  $\mathbb{R}^2$  centered at the origin with radius  $R$ , and  $h > 0$ . We obtain*

$$(2.6) \quad \int_{\Omega} |W_f| dx dy = 4\pi R, \quad W_f = \nabla \frac{1}{\sqrt{1+|\nabla f|^2}} \cdot \nabla f + \frac{1}{\sqrt{1+|\nabla f|^2}} \nabla^2 f.$$

*Proof.* Referring to the Lemma 2.1 in [52], we need to calculate the integral  $\int_{\Omega} |W_u| dx dy$  to approach  $\int_{\Omega} |W_f| dx dy$  for  $u \in \mathbf{S}$ . The functions  $u$  in the set  $\mathbf{S}$  are defined as follows:

$$\begin{aligned} \mathbf{S} &= \left\{ u \in \mathbf{C}^2[0, 2R] : u''(x) \leq 0 \text{ if } x \in (0, R), u''(x) \geq 0 \text{ if } x \in (R, 2R); \right. \\ &\quad \text{there exist two numbers } R_1, R_2, 0 < R_1 < R < R_2 < 2R, \text{ such that} \\ &\quad \left. u(x) = h \text{ if } x \in [0, R_1] \text{ and } u(x) = 0 \text{ if } x \in [R_2, 2R]; u'(R) < -\frac{2h}{R} \right\}. \end{aligned}$$

If  $u \in \mathbf{S}$ , for the radial symmetric surface  $z = u(r)$  with  $r = \sqrt{x^2 + y^2}$ , in order to eliminate the ambiguity of notation, we denote  $u(x, y) = u(\sqrt{x^2 + y^2})$ . Then we have

$$u_x = u' \frac{x}{r}, \quad u_y = u' \frac{y}{r}, \quad u_{xx} = u'' \frac{x^2}{r^2} + u' \frac{y^2}{r^3}, \quad u_{yy} = u'' \frac{y^2}{r^2} + u' \frac{x^2}{r^3}, \quad u_{xy} = u'' \frac{xy}{r^2} - u' \frac{xy}{r^3}.$$

Therefore, as the *Weingarten map* of a surface  $z = u(x, y)$  takes the form

$$\begin{aligned} W_u &= \nabla \frac{1}{\sqrt{1+|\nabla u|^2}} \cdot \nabla u + \frac{1}{\sqrt{1+|\nabla u|^2}} \nabla^2 u \\ &= \begin{bmatrix} \frac{u'' \frac{x^2}{r^2} + u' \frac{y^2}{r^3} (1+(u')^2)}{(1+(u')^2)^{3/2}} & \frac{u'' \frac{xy}{r^2} - u' \frac{xy}{r^3} (1+(u')^2)}{(1+(u')^2)^{3/2}} \\ \frac{u'' \frac{xy}{r^2} - u' \frac{xy}{r^3} (1+(u')^2)}{(1+(u')^2)^{3/2}} & \frac{u'' \frac{y^2}{r^2} + u' \frac{x^2}{r^3} (1+(u')^2)}{(1+(u')^2)^{3/2}} \end{bmatrix}. \end{aligned}$$

For a radial symmetric surface represented by  $z = u(r) = u(\sqrt{x^2 + y^2})$ , the *Weingarten map* can be rewritten as follows

$$(2.7) \quad |W_u| = \sqrt{\left(\frac{u''}{(\sqrt{1+(u')^2})^3}\right)^2 + \left(\frac{u'}{r\sqrt{1+(u')^2}}\right)^2},$$

with  $u' = u'(r)$ . Correspondingly, we obtain the following result:

$$(2.8) \quad \begin{aligned} \int_{\Omega} |W_u| dx dy &= \int_0^{2\pi} d\theta \int_0^{2R} r |W_u| dr \\ &= 2\pi \int_0^{2R} r \sqrt{\left(\frac{u''}{(\sqrt{1+(u')^2})^3}\right)^2 + \left(\frac{u'}{r\sqrt{1+(u')^2}}\right)^2} dr. \end{aligned}$$

If  $u \in \mathbf{S}$ , one can see that  $u'' \leq 0$  and  $u' \leq 0$  for  $r \in [0, R)$ , we obtain

$$\left| \frac{u''}{(\sqrt{1+(u')^2})^3} - \frac{u'}{r\sqrt{1+(u')^2}} \right| \leq |W_u| \leq \left| \frac{u''}{(\sqrt{1+(u')^2})^3} + \frac{u'}{r\sqrt{1+(u')^2}} \right|.$$

Note that  $\frac{u''}{(\sqrt{1+(u')^2})^3} = \left[ \frac{u'}{\sqrt{1+(u')^2}} \right]'$  and  $\frac{u''}{(\sqrt{1+(u')^2})^3} + \frac{u'}{r\sqrt{1+(u')^2}} = \frac{1}{r} \left[ r \frac{u'}{\sqrt{1+(u')^2}} \right]'$ , one gets

$$\begin{aligned} &\int_0^R r \left| \frac{u''}{(\sqrt{1+(u')^2})^3} - \frac{u'}{r\sqrt{1+(u')^2}} \right| dr \\ &\geq \int_0^R r \left| \frac{u''}{(\sqrt{1+(u')^2})^3} \right| dr - \int_0^R \left| \frac{u'}{\sqrt{1+(u')^2}} \right| dr \\ &= - \int_0^R r \left[ \frac{u'}{\sqrt{1+(u')^2}} \right]' dr + \int_0^R \frac{u'}{\sqrt{1+(u')^2}} dr \\ &= -R \frac{u'(R)}{\sqrt{1+(u'(R))^2}} + 2 \int_0^R \frac{u'}{\sqrt{1+(u')^2}} dr, \end{aligned}$$

and

$$\begin{aligned} \int_0^R r \left| \frac{u''}{(\sqrt{1+(u')^2})^3} + \frac{u'}{r\sqrt{1+(u')^2}} \right| dr &= \int_0^R \left| \left[ r \frac{u'}{\sqrt{1+(u')^2}} \right]' \right| dr \\ &= - \int_0^R \left[ r \frac{u'}{\sqrt{1+(u')^2}} \right]' dr \\ &= -R \frac{u'(R)}{\sqrt{1+(u'(R))^2}}. \end{aligned}$$

Thus we have

$$(2.9) \quad -R \frac{u'(R)}{\sqrt{1+(u'(R))^2}} + 2 \int_0^R \frac{u'}{\sqrt{1+(u')^2}} dr \leq \int_0^R r |W_u| dr \leq -R \frac{u'(R)}{\sqrt{1+(u'(R))^2}}.$$

When  $r \in (R, 2R)$ ,  $u'' \geq 0$  and  $u' \leq 0$ , we get

$$\left| \frac{u''}{(\sqrt{1+(u')^2})^3} + \frac{u'}{r\sqrt{1+(u')^2}} \right| \leq |W_u| \leq \left| \frac{u''}{(\sqrt{1+(u')^2})^3} - \frac{u'}{r\sqrt{1+(u')^2}} \right|,$$

where

$$\begin{aligned} \int_R^{2R} r \left| \frac{u''}{(\sqrt{1+(u')^2})^3} + \frac{u'}{r\sqrt{1+(u')^2}} \right| dr &= \int_R^{2R} \left| \left[ r \frac{u'}{\sqrt{1+(u')^2}} \right]' \right| dr \\ &\geq -R \frac{u'(R)}{\sqrt{1+(u'(R))^2}}, \end{aligned}$$

and

$$\begin{aligned} &\int_R^{2R} r \left| \frac{u''}{(\sqrt{1+(u')^2})^3} - \frac{u'}{r\sqrt{1+(u')^2}} \right| dr \\ &= \int_R^{2R} r \left[ \frac{u'}{\sqrt{1+(u')^2}} \right]' dr - \int_R^{2R} \frac{u'}{\sqrt{1+(u')^2}} dr \\ &= -R \frac{u'(R)}{\sqrt{1+(u'(R))^2}} - 2 \int_R^{2R} \frac{u'}{\sqrt{1+(u')^2}} dr. \end{aligned}$$

It follows that

$$(2.10) \quad -R \frac{u'(R)}{\sqrt{1+(u'(R))^2}} \leq \int_R^{2R} r |W_u| dr \leq -R \frac{u'(R)}{\sqrt{1+(u'(R))^2}} - 2 \int_R^{2R} \frac{u'}{\sqrt{1+(u')^2}} dr.$$

Based on (2.8), adding the formulas (2.9) and (2.10), we obtain the following inequalities:

$$(2.11) \quad \begin{aligned} &-4\pi R \frac{u'(R)}{\sqrt{1+(u'(R))^2}} + 4\pi \int_0^R \frac{u'}{\sqrt{1+(u')^2}} dr \\ &\leq \int_{\Omega} |W_u| dx dy \leq -4\pi R \frac{u'(R)}{\sqrt{1+(u'(R))^2}} - 4\pi \int_R^{2R} \frac{u'}{\sqrt{1+(u')^2}} dr. \end{aligned}$$

Considering  $\{u_n\} \in \mathbf{S}$  is any sequence of functions that pointwise converges to  $f = h_{\chi_{B(0,R)}}$ , it is easy to obtain that  $u'_n(R) \rightarrow -\infty$  and  $u'_n(r) \rightarrow 0$  with  $r \neq R$  when  $n \rightarrow +\infty$ . In addition, through the dominated convergence theorem, we have

$$(2.12) \quad \lim_{n \rightarrow +\infty} \int_0^R \frac{u'_n}{\sqrt{1+(u'_n)^2}} dr = \lim_{n \rightarrow +\infty} \int_R^{2R} \frac{u'_n}{\sqrt{1+(u'_n)^2}} dr = 0.$$

Moreover, according to the inequalities (2.11), there is

$$\lim_{n \rightarrow +\infty} \int_{\Omega} |W_{u_n}| dx dy = 4\pi R.$$

Therefore, we obtain the following integral:

$$(2.13) \quad \int_{\Omega} |W_f| dx dy = 4\pi R.$$

□

**REMARK 2.1.** *The integral gives twice as much as the mean curvature regularizer, both of which do not rely on heights of signals. This is an important property of the regularizer and will be used to demonstrate the restoration model with our regularizer can preserve image contrast. In contrast, the integral of total variation gives  $\int_{\Omega} |\nabla f| dx dy = 2\pi Rh$ , where the height  $h$  directly affects the value of the integral.*

**2.2. Spatially adapted first and second order regularization.** Although the proposed regularizer (2.5) has good geometric attributes, it is also highly non-convex and nonlinear. Indeed, we can further reformulate it based on the well-known Minkowski's inequality and Cauchy-Schwarz inequality as follows

$$\begin{aligned} \int_{\Omega} |W_u| dx &= \int_{\Omega} \left| \nabla \frac{1}{\sqrt{1+|\nabla u|^2}} \cdot \nabla u + \frac{1}{\sqrt{1+|\nabla u|^2}} \nabla^2 u \right| dx \\ &\leq \int_{\Omega} \left| \nabla \frac{1}{\sqrt{1+|\nabla u|^2}} \cdot \nabla u \right| dx + \int_{\Omega} \left| \frac{1}{\sqrt{1+|\nabla u|^2}} \nabla^2 u \right| dx \\ &\leq \int_{\Omega} \left| \nabla \frac{1}{\sqrt{1+|\nabla u|^2}} \right| |\nabla u| dx + \int_{\Omega} \frac{1}{\sqrt{1+|\nabla u|^2}} |\nabla^2 u| dx. \end{aligned}$$

Based on the above combined first and second order regularizer, we propose a novel variational model for image restoration by integrating the  $L^2$  norm data fidelity as follows

$$(2.14) \quad \min_u \int_{\Omega} \alpha(u) |\nabla u| dx + \int_{\Omega} \beta(u) |\nabla^2 u| dx + \frac{1}{2\lambda} \int_{\Omega} (u-f)^2 dx,$$

with

$$(2.15) \quad \alpha(u) = \left| \nabla \frac{1}{\sqrt{1+|\nabla u|^2}} \right|, \quad \text{and} \quad \beta(u) = \frac{1}{\sqrt{1+|\nabla u|^2}}.$$

Similar discussion can be applied to the data fidelity  $\int_{\Omega} (u-f)^2 dx$  in (2.14) to obtain the following lower bound result.

**Lemma 2.3.** *Assume  $f = h_{\chi_{B(0,R)}}(x,y)$  is an image defined on a rectangle  $\Omega = (-2R, 2R) \times (-2R, 2R)$ , where  $\chi$  represents the characteristic function,  $B(0, R)$  denotes an open disk in  $\mathbb{R}^2$  centered at the origin with radius  $R$ , and  $h > 0$ . Let  $u \in \mathbf{S}$  be an arbitrary smooth radial symmetric function. We have*

$$\int_{\Omega} (f-u)^2 dx dy \geq -\frac{\pi h^3}{12u'(R)} R.$$

*Proof.* This proof can be referred to the Theorem 2.2 in [52].  $\square$

With the conclusion of Lemma 2.2 and Lemma 2.3, we can further prove that  $f = h_{\chi_{B(0,R)}}$  is a minimizer of our model (2.14) as long as  $\lambda$  is chosen to be small enough, which means our model can preserve image contrast for image denoising. The claim is presented in the following theorem.

**Theorem 2.4.** *Let  $f = h_{\chi_{B(0,R)}}(x,y)$  be an image defined on a rectangle  $\Omega = (-2R, 2R) \times (-2R, 2R)$ , then there exists a constant  $C > 0$  such that if  $\lambda < C$ ,  $f$  attains the infimum of the proposed model (2.14) inside the function set  $\mathbf{S}$ , that is  $E(f) = \inf_{u \in \mathbf{S}} E(u)$ .*

*Proof.* Using Lemma 2.2 and Lemma 2.3, we have

$$\begin{aligned} (2.16) \quad E(u) &= \int_{\Omega} \alpha(u) |\nabla u| dx dy + \int_{\Omega} \beta(u) |\nabla^2 u| dx dy + \frac{1}{2\lambda} \int_{\Omega} (f-u)^2 dx dy \\ &> -4\pi R \frac{u'(R)}{\sqrt{1+(u'(R))^2}} - \frac{\pi h^3}{24\lambda u'(R)} R \\ &= 4\pi R \frac{(-u'(R))}{\sqrt{1+(-u'(R))^2}} + \frac{\pi h^3}{24\lambda(-u'(R))} R. \end{aligned}$$

Especially, we consider the function  $y(x) = \frac{c_1 x}{\sqrt{1+x^2}} + \frac{c_2}{\lambda x}$  defined on  $[\frac{2h}{R}, +\infty)$ , where  $c_1, c_2$  are positive constants. Then there is

$$\begin{aligned} y'(x) &= \frac{c_1}{(1+x^2)^{3/2}} - \frac{c_2}{\lambda x^2} \\ &\leq \frac{c_1}{x^3} \left(1 - \frac{c_2}{\lambda c_1} x\right). \end{aligned}$$

If  $\lambda < \frac{c_2}{c_1} \frac{2h}{R}$ ,  $y'(x) < 0$  for any  $x \in [\frac{2h}{R}, +\infty)$ . One can see that  $\lim_{x \rightarrow +\infty} y(x) = c_1$ , which means  $y(x)$  will strictly decrease to  $c_1$  on  $[\frac{2h}{R}, +\infty)$ .

We set  $c_1 = 4\pi R$  and  $c_2 = \frac{\pi h^3 R}{24}$  in (2.16). Hence, when  $\lambda < \frac{c_2}{c_1} \frac{2h}{R} = \frac{h^4}{48R} = C$  in our proposed model,  $E(u) > c_1 = 4\pi R = E(f)$  for any smooth function  $u \in \mathbf{S}$ . Furthermore, a smooth function  $u \in \mathbf{S}$  satisfying  $E(u) - \varepsilon < E(f) < E(u)$  can be found for arbitrary small  $\varepsilon > 0$ , we obtain that  $E(f) = \inf_{u \in \mathbf{S}} E(u)$  if  $\lambda < \frac{h^4}{48R}$ . This demonstrates that the proposed model (2.14) can keep the image contrast when  $\lambda$  is small enough.  $\square$

REMARK 2.2. *This theorem indicates that our proposed model (2.14) can keep the image contrast once  $\lambda$  is small enough. In contrast, according to [43], when  $\lambda < \frac{h}{R}$ , the ROF functional  $E(u) = \lambda \int_{\Omega} |\nabla u| dx dy + \int_{\Omega} (f - u)^2 dx dy$  can approach the minimizer  $u = (h - \lambda R) \chi_{B(0, R)}$ , which means that the ROF model will lose image contrast no matter how small  $\lambda$  is.*

REMARK 2.3. *The theorem also indicates that our proposed model (2.14) can keep sharp edges, which is another important property for image denoising.*

**3. Numerical algorithm.** Because  $\alpha(u)$  and  $\beta(u)$  in (2.14) are functions of  $u$  and unknown in principle, the optimality condition will lead to a highly nonlinear fourth order partial differential equation (PDE). In order to avoid to solve the fourth order evolution equation, we explore considering the proposed model (2.14) as a weighted first and second order minimization problem. It can be observed that  $\beta(u)$  is small at edges and large at smooth regions, acting as the edge detector function. Once  $\beta(u)$  is obtained,  $\alpha(u)$  can be directly estimated as the variation of  $\beta(u)$ . Thus, the main task is to derive  $\beta(u)$  in our model.

Bresson *et al.* [9] introduced the edge detector function as the weight for TV minimization, which estimates the edge detection function using the observed image through  $\beta(f) = \frac{1}{1+|\nabla f|^2}$ . Indeed, if the clean/solution image  $u^*$  is available, we can compute  $\beta(u^*) = \frac{1}{1+|\nabla u^*|^2}$ . For these two cases, both  $\alpha(u)$  and  $\beta(u)$  in (2.14) are spatially varying weights independent of  $u$ , in which case the minimization (2.14) becomes convex and can be solved by convex optimization methods. On the other hand, we can estimate  $\alpha(u)$  and  $\beta(u)$  using the latest  $u$  in the iterative scheme which means both of them are updated in a dynamical way.

Fig. 2 presents the denoising results of the spatially adapted first and second order regularized model (2.14), where we use the observed image (Fig. 2 (b)), dynamical update (Fig. 2 (c)) and the clean image (Fig. 2 (d)) to estimate the weight functions. It is clearly shown that the best recovery result is obtained by using the weight functions achieved by the clean image, and the dynamical update for the weight functions also gives the satisfactory results compared to the one obtained by the noisy image. Of course, there is no clean images for real applications. Thus, we use the dynamical update to balance the recovery results and computational efficiency.

**3.1. Constrained optimization and ADMM.** For the algorithm, we solve the minimization problem (2.14) with a separate step of evaluating  $\alpha(u)$  and  $\beta(u)$ .

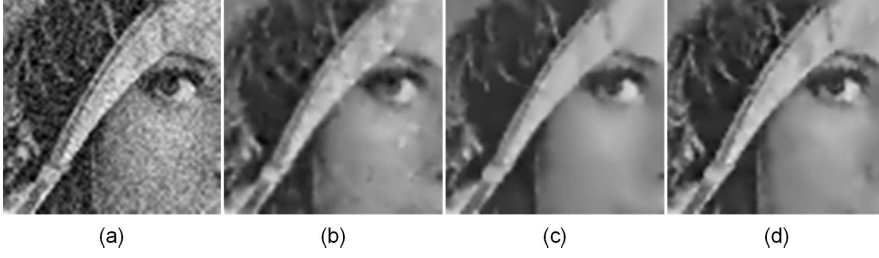


FIG. 2. Denoising results of “lena” by the proposed model (2.14). From left to right: (a) Gaussian noisy image with mean 0 and variance  $\sigma = 20$ , (b) the recovery result using the noisy image to estimate the weight functions, (c) the recovery result using dynamical update to estimate the weight functions, (d) the recovery result using the clean image to estimate the weight functions, respectively.

Specially, we introduce two auxiliary variables  $v$  and  $w$  and rewrite the original unconstrained optimization problem (2.14) into a constrained version as follows

$$(3.1) \quad \begin{aligned} \min_{u,v,w} \quad & \int_{\Omega} \alpha(u)|v|dx + \int_{\Omega} \beta(u)|w|dx + \frac{1}{2\lambda} \int_{\Omega} (u-f)^2 dx \\ \text{s.t.} \quad & v = \nabla u, \quad w = \nabla^2 u. \end{aligned}$$

Given some  $(u^k, v^k, w^k) \in \mathbb{R}^n \times \mathbb{R}^{n^2} \times \mathbb{R}^{n^4}$ , the proximal augmented Lagrangian functional is defined as follows

$$(3.2) \quad \begin{aligned} \mathcal{L}(u, v, w; \lambda_1, \lambda_2) = & \int_{\Omega} \alpha(u)|v|dx + \int_{\Omega} \beta(u)|w|dx + \frac{1}{2\lambda} \int_{\Omega} (u-f)^2 dx \\ & + \frac{r_1}{2} \int_{\Omega} (v - \nabla u - \frac{\lambda_1}{r_1})^2 dx + \frac{r_2}{2} \int_{\Omega} (w - \nabla^2 u - \frac{\lambda_2}{r_2})^2 dx \\ & + \frac{\mu}{2} \int_{\Omega} (u - u^k)^2 dx + \frac{\gamma}{2} \int_{\Omega} (v - v^k)^2 dx + \frac{\tau}{2} \int_{\Omega} (w - w^k)^2 dx, \end{aligned}$$

where  $\lambda_1, \lambda_2$  are the Lagrange multipliers, and  $r_1, r_2, \mu, \gamma, \tau$  are the positive penalty parameters. During each iteration, by the alternating direction method of multipliers, we tend to sequentially minimize (3.2) over variables  $(u, v, w)$  while keeping the reminder variables fixed. The minimizers  $u^{k+1}, v^{k+1}, w^{k+1}$  are gives from

$$(3.3) \quad \left\{ \begin{aligned} u^{k+1} = \arg \min_u \quad & \frac{1}{2\lambda} \int_{\Omega} (u-f)^2 dx + \frac{r_1}{2} \int_{\Omega} (\nabla u - (v^k - \frac{\lambda_1^k}{r_1}))^2 dx \\ & + \frac{r_2}{2} \int_{\Omega} (\nabla^2 u - (w^k - \frac{\lambda_2^k}{r_2}))^2 dx + \frac{\mu}{2} \int_{\Omega} (u - u^k)^2 dx, \\ v^{k+1} = \arg \min_v \quad & \int_{\Omega} \alpha(u^{k+1})|v|dx + \frac{r_1}{2} \int_{\Omega} (v - \nabla u^{k+1} - \frac{\lambda_1^k}{r_1})^2 dx \\ & + \frac{\gamma}{2} \int_{\Omega} (v - v^k)^2 dx, \\ w^{k+1} = \arg \min_w \quad & \int_{\Omega} \beta(u^{k+1})|w|dx + \frac{r_2}{2} \int_{\Omega} (w - \nabla^2 u^{k+1} - \frac{\lambda_2^k}{r_2})^2 dx \\ & + \frac{\tau}{2} \int_{\Omega} (w - w^k)^2 dx, \end{aligned} \right.$$

and then update the Lagrange multipliers  $(\lambda_1, \lambda_2)$  through a standard dual-ascent rule from

$$(3.4) \quad \begin{cases} \lambda_1^{k+1} = \lambda_1^k + r_1(\nabla u^{k+1} - v^{k+1}), \\ \lambda_2^{k+1} = \lambda_2^k + r_2(\nabla^2 u^{k+1} - w^{k+1}), \end{cases}$$

where both  $\alpha(u^{k+1})$  and  $\beta(u^{k+1})$  are of known values as

$$(3.5) \quad \alpha(u^{k+1}) = \left| \nabla \frac{1}{\sqrt{1 + |\nabla u^{k+1}|^2}} \right| \quad \text{and} \quad \beta(u^{k+1}) = \frac{1}{\sqrt{1 + |\nabla u^{k+1}|^2}}.$$

**REMARK 3.1.** *We introduce the proximal terms  $\frac{\mu}{2} \int_{\Omega} (u - u^k)^2 dx$ ,  $\frac{\gamma}{2} \int_{\Omega} (v - v^k)^2 dx$  and  $\frac{\tau}{2} \int_{\Omega} (w - w^k)^2 dx$  into the  $u, v$  and  $w$  subproblems to guarantee the convergence of the proposed numerical algorithm in theory, the parameters  $\mu, \gamma$  and  $\tau$  of which are all set to zero in numerical implementations.*

### 3.2. Subproblems.

**3.2.1. The sub-minimization problem w.r.t.  $u$ .** Given the fixed variables  $v^k, w^k, \lambda_1^k, \lambda_2^k$  at the  $(k+1)$ -th outer iteration, the  $u$ -subproblem can be easily derived by differentiating with respect to  $u$  and setting the result equal to zero. That is the corresponding solution is obtained by considering the following first-order necessary optimality condition, i.e.,

$$\frac{1}{\lambda}(u^{k+1} - f) - r_1 \operatorname{div}(\nabla u^{k+1} - v^k + \frac{\lambda_1^k}{r_1}) + r_2 \operatorname{div}^2(\nabla^2 u^{k+1} - w^k + \frac{\lambda_2^k}{r_2}) + \mu(u^{k+1} - u^k) = 0,$$

which can be simplified as

$$\left( \frac{1}{\lambda} \mathcal{I} - r_1 \Delta + r_2 \Delta^2 + \mu \right) u^{k+1} = \frac{f}{\lambda} - \operatorname{div}(r_1 v^k - \lambda_1^k) + \operatorname{div}^2(r_2 w^k - \lambda_2^k) + \mu u^k,$$

with  $\mathcal{I}$  being the identity matrix and  $\Delta^2 = \operatorname{div}^2 \nabla^2$ . As long as the periodic boundary condition is adopted, we can utilize the fast Fourier transform (FFT) to obtain the optimal solution  $u^{k+1}$  from

$$(3.6) \quad u^{k+1} = \mathcal{F}^{-1} \left( \frac{\mathcal{F}(f/\lambda - \operatorname{div}(r_1 v^k - \lambda_1^k) + \operatorname{div}^2(r_2 w^k - \lambda_2^k) + \mu u^k)}{(1/\lambda + \mu)\mathcal{I} - r_1 \mathcal{F} \Delta \mathcal{F}^{-1} + r_2 \mathcal{F} \Delta^2 \mathcal{F}^{-1}} \right),$$

where  $\mathcal{F}$  and  $\mathcal{F}^{-1}$  represent the commonly-used forward and inverse FFT operation, respectively.

**3.2.2. The sub-minimization problem w.r.t.  $(v, w)$ .** The solutions of  $(v, w)$ -subproblems in (3.3) can be easily generated using the popular shrinkage operator [3, 6] as follows

$$(3.7) \quad v^{k+1} = (v_1^{k+1}, v_2^{k+1}) = \operatorname{shrinkage} \left( \frac{r_1 \nabla u^{k+1} + \lambda_1^k + \gamma v^k}{r_1 + \gamma}, \frac{\alpha(u^{k+1})}{r_1 + \gamma} \right),$$

and

$$(3.8) \quad w^{k+1} = (w_{11}^{k+1}, w_{12}^{k+1}, w_{21}^{k+1}, w_{22}^{k+1}) = \operatorname{shrinkage} \left( \frac{r_2 \nabla^2 u^{k+1} + \lambda_2^k + \tau w^k}{r_2 + \tau}, \frac{\beta(u^{k+1})}{r_2 + \tau} \right),$$

where the shrinkage operator is defined as

$$\text{shrinkage}(a, b) = \max\{|a| - b, 0\} \circ \frac{a}{|a|}$$

with  $\circ$  denoting the point-wise multiplication.

In brief, an efficient ADMM-based numerical algorithm is proposed to deal with the hybrid spatially adapted variational model (2.14). The optimization procedure of the proposed method is summarized as Algorithm 1.

---

### ADMM for Spatially Adapted First and Second Order Variational Model

---

- 1: **Input:** Degraded image  $f$ , positive constant  $\lambda$ , penalty factors  $(r_1, r_2)$ , maximum iteration  $K_{\max}$ , and stopping threshold  $\epsilon$ ;
  - 2: **Initialize:**  $u^0 = f$  and  $v^0 = w^0 = \lambda_1^0 = \lambda_2^0 = 0$ , set  $k = 0$ ;
  - 3: **while** (not converged and  $k \leq K_{\max}$ )
  - 4:   Compute  $u^{k+1}$  from Eq. (3.6) for fixed  $v^k, w^k, \lambda_1^k$  and  $\lambda_2^k$ ;
  - 5:   Update  $\alpha(u^{k+1})$  and  $\beta(u^{k+1})$  using  $u^{k+1}$  according to Eq. (3.5);
  - 6:   Compute  $v^{k+1}$  from Eq. (3.7) for fixed  $u^{k+1}$  and  $\lambda_1^k$ ;
  - 7:   Compute  $w^{k+1}$  from Eq. (3.8) for fixed  $u^{k+1}$  and  $\lambda_2^k$ ;
  - 8:   Update  $\lambda_1^{k+1}$  and  $\lambda_2^{k+1}$  according to (3.4);
  - 9:   Check convergence condition:  $\|u^{k+1} - u^k\|_1 / \|u^k\|_1 \leq \epsilon$ ;
  - 10: **end while**
  - 11: **Output:** Reconstructed image  $u$ .
- 

**3.3. Convergence Analysis.** In this subsection, we give the theoretical analysis for the proposed ADMM-based numerical algorithm under certain conditions.

**Theorem 3.1.** *Let  $\{u^k, v^k, w^k, \lambda_1^k, \lambda_2^k\}_{k \in \mathbb{N}}$  be the sequence generated by the proposed ADMM-numerical algorithm and  $(\bar{u}, \bar{v}, \bar{w}, \bar{\lambda}_1, \bar{\lambda}_2)$  be a point satisfying the first-order optimality conditions,*

$$(3.9) \quad \begin{cases} (u - f)/\lambda - \text{div}\lambda_1 + \text{div}^2\lambda_2 = 0, \\ \alpha(u)s - \lambda_1 = 0, \quad s \in \partial|v| \text{ and } \alpha(u) = \left| \nabla \frac{1}{\sqrt{1+|\nabla u|^2}} \right|, \\ \beta(u)p - \lambda_2 = 0, \quad p \in \partial|w| \text{ and } \beta(u) = \frac{1}{\sqrt{1+|\nabla u|^2}}, \\ \nabla u - v = 0, \quad \nabla^2 u - w = 0. \end{cases}$$

Let  $u_e^k = u^k - \bar{u}, v_e^k = v^k - \bar{v}, w_e^k = w^k - \bar{w}, \lambda_{1e}^k = \lambda_1^k - \bar{\lambda}_1, \lambda_{2e}^k = \lambda_2^k - \bar{\lambda}_2$  denote the error sequences. If for any  $s^k \in \partial|v^k|, \bar{s} \in \partial|\bar{v}|$  and  $p^k \in \partial|w^k|, \bar{p} \in \partial|\bar{w}|$  the quantity

$$(3.10) \quad \begin{cases} \Delta_1^k := \langle (\alpha(u^k) - \alpha(\bar{u}))s^k, v^k - \bar{v} \rangle, \quad \alpha(\bar{u}) = \left| \nabla \frac{1}{\sqrt{1+|\nabla \bar{u}|^2}} \right|, \\ \Delta_2^k := \langle (\beta(u^k) - \beta(\bar{u}))p^k, w^k - \bar{w} \rangle, \quad \beta(\bar{u}) = \frac{1}{\sqrt{1+|\nabla \bar{u}|^2}}, \end{cases}$$

is nonnegative, then the following holds:

- (a) The sequence  $\{e_k\}_{k \in \mathbb{N}}$  defined by

$$(3.11) \quad e_k := \frac{\mu}{2} \|u_e^k\|^2 + \frac{r_1 + \gamma}{2} \|v_e^k\|^2 + \frac{r_2 + \tau}{2} \|w_e^k\|^2 + \frac{1}{2r_1} \|\lambda_{1e}^k\|^2 + \frac{1}{2r_2} \|\lambda_{2e}^k\|^2,$$

is monotonically decreasing.

(b) The residuals  $\|\nabla u^{k+1} - v^k\|, \|\nabla^2 u^{k+1} - w^k\|, \|u^{k+1} - u^k\|, \|v^{k+1} - v^k\|, \|w^{k+1} - w^k\|, \|\lambda_1^{k+1} - \lambda_1^k\|, \|\lambda_2^{k+1} - \lambda_2^k\|$  converge to zero in  $L^2(\Omega)$  as  $k$  approaches infinity.

(c) *The generated sequence  $\{(u^k, v^k, w^k, \lambda_1^k, \lambda_2^k)\}_{k \in \mathbb{N}}$  converges to a limit point  $(u^*, v^*, w^*, \lambda_1^*, \lambda_2^*)$  that satisfies the first-order optimality conditions (3.9).*

*Proof.* First, the part (a) is proved by the introduced error sequences. Note that the optimality conditions of subproblems in our proposed algorithm can be indicated as follows

$$(3.12) \quad \begin{cases} (u^{k+1} - f)/\lambda - r_1 \operatorname{div}(\nabla u^{k+1} - (v^k - \frac{\lambda_1^k}{r_1})) \\ \quad + r_2 \operatorname{div}^2(\nabla^2 u^{k+1} - (w^k - \frac{\lambda_2^k}{r_2})) + \mu(u^{k+1} - u^k) = 0, \\ \alpha(u^{k+1})s^{k+1} + r_1(v^{k+1} - \nabla u^{k+1} - \frac{\lambda_1^k}{r_1}) + \gamma(v^{k+1} - v^k) = 0, \\ \beta(u^{k+1})p^{k+1} + r_2(w^{k+1} - \nabla^2 u^{k+1} - \frac{\lambda_2^k}{r_2}) + \tau(w^{k+1} - w^k) = 0, \\ \lambda_1^{k+1} = \lambda_1^k + r_1(\nabla u^{k+1} - v^{k+1}), \\ \lambda_2^{k+1} = \lambda_2^k + r_2(\nabla^2 u^{k+1} - w^{k+1}). \end{cases}$$

Then, we express these equations in the form of errors, i.e.,

$$\begin{cases} u_e^{k+1}/\lambda - r_1 \operatorname{div}(\nabla u_e^{k+1} - v_e^k) - \operatorname{div} \lambda_{1e}^k + r_2 \operatorname{div}^2(\nabla^2 u_e^{k+1} - w_e^k) \\ \quad + \operatorname{div}^2 \lambda_{2e}^k + \mu(u_e^{k+1} - u_e^k) = 0, \\ \alpha(u^{k+1})s^{k+1} - \alpha(\bar{u})\bar{s} + r_1(v_e^{k+1} - \nabla u_e^{k+1}) - \lambda_{1e}^k + \gamma(v_e^{k+1} - v_e^k) = 0, \\ \beta(u^{k+1})p^{k+1} - \beta(\bar{u})\bar{p} + r_2(w_e^{k+1} - \nabla^2 u_e^{k+1}) - \lambda_{2e}^k + \tau(w_e^{k+1} - w_e^k) = 0, \\ \lambda_{1e}^{k+1} = \lambda_{1e}^k + r_1(\nabla u_e^{k+1} - v_e^{k+1}), \\ \lambda_{2e}^{k+1} = \lambda_{2e}^k + r_2(\nabla^2 u_e^{k+1} - w_e^{k+1}). \end{cases}$$

Furthermore, we take the inner product of each equation respectively with  $u_e^{k+1}$ ,  $v_e^{k+1}$ ,  $w_e^{k+1}$ ,  $\lambda_{1e}^k$  and  $\lambda_{2e}^k$ , i.e.,

$$\begin{cases} \|u_e^{k+1}\|^2/\lambda + r_1 \langle \nabla u_e^{k+1} - v_e^k, \nabla u_e^{k+1} \rangle + r_2 \langle \nabla^2 u_e^{k+1} - w_e^k, \nabla^2 u_e^{k+1} \rangle \\ \quad + \mu \langle u_e^{k+1} - u_e^k, u_e^{k+1} \rangle = -\langle \lambda_{1e}^k, \nabla u_e^{k+1} \rangle - \langle \lambda_{2e}^k, \nabla^2 u_e^{k+1} \rangle, \\ \langle \alpha(u^{k+1})s^{k+1} - \alpha(\bar{u})\bar{s}, v_e^{k+1} \rangle + r_1 \langle v_e^{k+1} - \nabla u_e^{k+1}, v_e^{k+1} \rangle + \gamma \langle v_e^{k+1} - v_e^k, v_e^{k+1} \rangle \\ \quad = \langle \lambda_{1e}^k, v_e^{k+1} \rangle, \\ \langle \beta(u^{k+1})p^{k+1} - \beta(\bar{u})\bar{p}, w_e^{k+1} \rangle + r_2 \langle w_e^{k+1} - \nabla^2 u_e^{k+1}, w_e^{k+1} \rangle + \tau \langle w_e^{k+1} - w_e^k, w_e^{k+1} \rangle \\ \quad = \langle \lambda_{2e}^k, w_e^{k+1} \rangle, \\ \langle \lambda_{1e}^{k+1} - \lambda_{1e}^k, \lambda_{1e}^k \rangle = r_1 \langle \nabla u_e^{k+1} - v_e^{k+1}, \lambda_{1e}^k \rangle, \\ \langle \lambda_{2e}^{k+1} - \lambda_{2e}^k, \lambda_{2e}^k \rangle = r_2 \langle \nabla^2 u_e^{k+1} - w_e^{k+1}, \lambda_{2e}^k \rangle. \end{cases}$$

According to the identity  $\langle v - w, v \rangle = \frac{1}{2}(\|v\|^2 + \|v - w\|^2 - \|w\|^2)$  in  $L^2(\Omega)$ , it follows that

$$\begin{cases} \|u_e^{k+1}\|^2/\lambda + \frac{r_1}{2}(\|\nabla u_e^{k+1}\|^2 + \|\nabla u_e^{k+1} - v_e^k\|^2 - \|v_e^k\|^2) \\ \quad + \frac{r_2}{2}(\|\nabla^2 u_e^{k+1}\|^2 + \|\nabla^2 u_e^{k+1} - w_e^k\|^2 - \|w_e^k\|^2) + \frac{\mu}{2}(\|u_e^{k+1}\|^2 + \|u_e^{k+1} - u_e^k\|^2 - \|u_e^k\|^2) \\ \quad = -\langle \lambda_{1e}^k, \nabla u_e^{k+1} \rangle - \langle \lambda_{2e}^k, \nabla^2 u_e^{k+1} \rangle, \\ \langle \alpha(u^{k+1})s^{k+1} - \alpha(\bar{u})\bar{s}, v_e^{k+1} \rangle + \frac{r_1}{2}(\|v_e^{k+1}\|^2 + \|v_e^{k+1} - \nabla u_e^{k+1}\|^2 - \|\nabla u_e^{k+1}\|^2) \\ \quad + \frac{\gamma}{2}(\|v_e^{k+1}\|^2 + \|v_e^{k+1} - v_e^k\|^2 - \|v_e^k\|^2) = \langle \lambda_{1e}^k, v_e^{k+1} \rangle, \\ \langle \beta(u^{k+1})p^{k+1} - \beta(\bar{u})\bar{p}, w_e^{k+1} \rangle + \frac{r_2}{2}(\|w_e^{k+1}\|^2 + \|w_e^{k+1} - \nabla^2 u_e^{k+1}\|^2 - \|\nabla^2 u_e^{k+1}\|^2) \\ \quad + \frac{\tau}{2}(\|w_e^{k+1}\|^2 + \|w_e^{k+1} - w_e^k\|^2 - \|w_e^k\|^2) = \langle \lambda_{2e}^k, w_e^{k+1} \rangle, \\ \frac{1}{2r_1} \|\lambda_{1e}^{k+1}\|^2 - \frac{1}{2r_1} \|\lambda_{1e}^k\|^2 - \frac{r_1}{2} \|v_e^{k+1} - \nabla u_e^{k+1}\|^2 = \langle \nabla u_e^{k+1} - v_e^{k+1}, \lambda_{1e}^k \rangle, \\ \frac{1}{2r_2} \|\lambda_{2e}^{k+1}\|^2 - \frac{1}{2r_2} \|\lambda_{2e}^k\|^2 - \frac{r_2}{2} \|w_e^{k+1} - \nabla^2 u_e^{k+1}\|^2 = \langle \nabla^2 u_e^{k+1} - w_e^{k+1}, \lambda_{2e}^k \rangle. \end{cases}$$

Finally, we add the right and left sides of these equations, i.e.,

$$\begin{aligned}
& \frac{\mu}{2} \|u_e^{k+1}\|^2 + \frac{r_1 + \gamma}{2} \|v_e^{k+1}\|^2 + \frac{r_2 + \tau}{2} \|w_e^{k+1}\|^2 + \frac{1}{2r_1} \|\lambda_{1e}^{k+1}\|^2 + \frac{1}{2r_2} \|\lambda_{2e}^{k+1}\|^2 \\
& + \frac{r_1}{2} \|\nabla u_e^{k+1} - v_e^k\|^2 + \frac{r_2}{2} \|\nabla^2 u_e^{k+1} - w_e^k\|^2 + \frac{\mu}{2} \|u^{k+1} - u^k\|^2 \\
& + \frac{\gamma}{2} \|v^{k+1} - v^k\|^2 + \frac{\tau}{2} \|w^{k+1} - w^k\|^2 + \|u_e^{k+1}\|^2 / \lambda \\
& + \langle \alpha(u^{k+1})s^{k+1} - \alpha(\bar{u})\bar{s}, v_e^{k+1} \rangle + \langle \beta(u^{k+1})p^{k+1} - \beta(\bar{u})\bar{p}, w_e^{k+1} \rangle \\
& = \frac{\mu}{2} \|u_e^k\|^2 + \frac{r_1 + \gamma}{2} \|v_e^k\|^2 + \frac{r_2 + \tau}{2} \|w_e^k\|^2 + \frac{1}{2r_1} \|\lambda_{1e}^k\|^2 + \frac{1}{2r_2} \|\lambda_{2e}^k\|^2.
\end{aligned}$$

In particular, note that  $\langle \alpha(u^{k+1})s^{k+1} - \alpha(\bar{u})\bar{s}, v_e^{k+1} \rangle = \Delta_1^{k+1} + \alpha(\bar{u})\langle s_e^{k+1}, v_e^{k+1} \rangle$  and  $\langle \beta(u^{k+1})p^{k+1} - \beta(\bar{u})\bar{p}, w_e^{k+1} \rangle = \Delta_2^{k+1} + \beta(\bar{u})\langle p_e^{k+1}, w_e^{k+1} \rangle$ . The inner product term  $\langle s_e^{k+1}, v_e^{k+1} \rangle \geq 0$ ,  $\langle p_e^{k+1}, w_e^{k+1} \rangle \geq 0$  for any  $s^k \in \partial|v^k|$ ,  $\bar{s} \in \partial|\bar{v}|$  and  $p^k \in \partial|w^k|$ ,  $\bar{p} \in \partial|\bar{w}|$  on the basis of Lemma 3.3 in [14]. In addition,  $\Delta_1, \Delta_2 \geq 0$  for all  $k$  according to the assumption of proposed theorem. Therefore,  $\langle \alpha(u^{k+1})s^{k+1} - \alpha(\bar{u})\bar{s}, v_e^{k+1} \rangle \geq 0$  and  $\langle \beta(u^{k+1})p^{k+1} - \beta(\bar{u})\bar{p}, w_e^{k+1} \rangle \geq 0$ . It is obvious that the term  $\|u_e^{k+1}\|^2 / \lambda \geq 0$  with  $\lambda > 0$ . We drop these three nonnegative terms to obtain

$$\begin{aligned}
(3.13) \quad e_{k+1} + \frac{r_1}{2} \|\nabla u_e^{k+1} - v_e^k\|^2 + \frac{r_2}{2} \|\nabla^2 u_e^{k+1} - w_e^k\|^2 \\
+ \frac{\mu}{2} \|u^{k+1} - u^k\|^2 + \frac{\gamma}{2} \|v^{k+1} - v^k\|^2 + \frac{\tau}{2} \|w^{k+1} - w^k\|^2 \leq e_k,
\end{aligned}$$

where  $e_k$  is defined in (3.11). Owing to the term  $\frac{r_1}{2} \|\nabla u_e^{k+1} - v_e^k\|^2 + \frac{r_2}{2} \|\nabla^2 u_e^{k+1} - w_e^k\|^2 + \frac{\mu}{2} \|u^{k+1} - u^k\|^2 + \frac{\gamma}{2} \|v^{k+1} - v^k\|^2 + \frac{\tau}{2} \|w^{k+1} - w^k\|^2 \geq 0$ , then the sequence  $\{e_k\}_{k \in \mathbb{N}}$  is monotone decreasing.

Next, we prove the part (b) according to the sequence  $\{e_k\}_{k \in \mathbb{N}}$ . Considering that  $\{e_k\}_{k \in \mathbb{N}}$  is nonnegative and monotone decreasing, we sum the inequality (3.13) from  $k = 0$  to infinity and obtain the inequality

$$\begin{aligned}
& \frac{r_1}{2} \sum_{k=0}^{\infty} \|\nabla u_e^{k+1} - v_e^k\|^2 + \frac{r_2}{2} \sum_{k=0}^{\infty} \|\nabla^2 u_e^{k+1} - w_e^k\|^2 + \frac{\mu}{2} \sum_{k=0}^{\infty} \|u^{k+1} - u^k\|^2 \\
& + \frac{\gamma}{2} \sum_{k=0}^{\infty} \|v^{k+1} - v^k\|^2 + \frac{\tau}{2} \sum_{k=0}^{\infty} \|w^{k+1} - w^k\|^2 \leq e_0 - e_{k+1} < \infty.
\end{aligned}$$

This further indicates

$$\begin{aligned}
(3.14) \quad \lim_{k \rightarrow \infty} (\|\nabla u_e^{k+1} - v_e^k\| = \|\nabla^2 u_e^{k+1} - w_e^k\| = \|u^{k+1} - u^k\| \\
= \|v^{k+1} - v^k\| = \|w^{k+1} - w^k\|) = 0.
\end{aligned}$$

Moreover, using the last two equalities in (3.12) and Minkowski's inequality, we obtain

$$\|\lambda_1^{k+1} - \lambda_1^k\| \leq (r_1 \|\nabla u_e^{k+1} - v_e^k\| + r_1 \|v^{k+1} - v^k\|) = 0,$$

$$\|\lambda_2^{k+1} - \lambda_2^k\| \leq (r_1 \|\nabla^2 u_e^{k+1} - w_e^k\| + r_1 \|w^{k+1} - w^k\|) = 0.$$

Thus, according to (3.14) we have

$$(3.15) \quad \lim_{k \rightarrow \infty} (\|\lambda_1^{k+1} - \lambda_1^k\| = \|\lambda_2^{k+1} - \lambda_2^k\|) = 0.$$

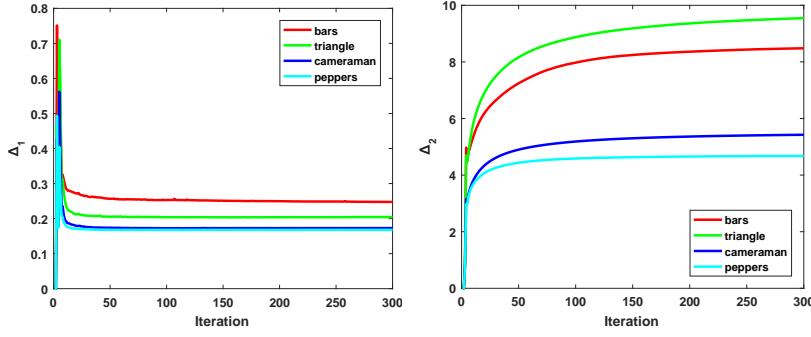


FIG. 3. The behavior of  $\Delta_1$  and  $\Delta_2$  versus iteration numbers on the test images showed in Fig. 4, which can be observe that  $\Delta_1 \geq 0$  and  $\Delta_2 \geq 0$  for all iterations.

Last, we prove part (c) by part (a) and part (b). Since the error term  $\{e_k\}_{k \in \mathbb{N}}$  is a monotone decreasing sequence in  $\mathbb{R}^+$  and for any point  $(\bar{u}, \bar{v}, \bar{w}, \bar{\lambda}_1, \bar{\lambda}_2)$  that satisfies (3.9). Moreover, according to (3.14) and (3.15), the sequence  $\{(u^k, v^k, w^k, \lambda_1^k, \lambda_2^k)\}_{k \in \mathbb{N}} \subset (L^2(\Omega))^5$  generated by our proposed algorithm is uniformly bounded in  $\Omega$ . Therefore, there exists a weakly convergent subsequence  $\{(u^{k_l}, v^{k_l}, w^{k_l}, \lambda_1^{k_l}, \lambda_2^{k_l})\}_{l \in \mathbb{N}}$ , which has a limit point  $(u^*, v^*, w^*, \lambda_1^*, \lambda_2^*)$ . Analogously, due to  $v^{k_l} \rightarrow v^*$ ,  $w^{k_l} \rightarrow w^*$  a.e. in  $\Omega$  as  $l \rightarrow \infty$  and  $s^{k_l} \in \partial|v^{k_l}|$ ,  $p^{k_l} \in \partial|w^{k_l}|$ , there exists a subsequence of  $\{s^{k_l}\}_{l \in \mathbb{N}}$  and  $\{p^{k_l}\}_{l \in \mathbb{N}}$  that converges weakly to  $s^* \in \partial|v^*|$  and  $p^* \in \partial|w^*|$  respectively.

The sequence  $\{(u^{k_l}, v^{k_l}, w^{k_l}, \lambda_1^{k_l}, \lambda_2^{k_l})\}_{l \in \mathbb{N}}$  satisfies the optimality conditions in (3.12), i.e.,

$$\begin{cases} (u^{k_l+1} - f)/\lambda - r_1 \operatorname{div}(\nabla u^{k_l+1} - (v^{k_l} - \frac{\lambda_1^{k_l}}{r_1})) \\ \quad + r_2 \operatorname{div}^2(\nabla^2 u^{k_l+1} - (w^{k_l} - \frac{\lambda_2^{k_l}}{r_2})) + \mu(u^{k_l+1} - u^{k_l}) = 0, \\ \alpha(u^{k_l+1})s^{k_l+1} + r_1(v^{k_l+1} - \nabla u^{k_l+1} - \frac{\lambda_1^{k_l}}{r_1}) + \gamma(v^{k_l+1} - v^{k_l}) = 0, \\ \beta(u^{k_l+1})p^{k_l+1} + r_2(w^{k_l+1} - \nabla^2 u^{k_l+1} - \frac{\lambda_2^{k_l}}{r_2}) + \tau(w^{k_l+1} - w^{k_l}) = 0, \\ \lambda_1^{k_l+1} = \lambda_1^{k_l} + r_1(\nabla u^{k_l+1} - v^{k_l+1}), \\ \lambda_2^{k_l+1} = \lambda_2^{k_l} + r_2(\nabla^2 u^{k_l+1} - w^{k_l+1}). \end{cases}$$

Taking the limit from the convergent subsequence, based on part (b) we obtain

$$\begin{cases} (u^* - f)/\lambda - \operatorname{div}\lambda_1^* + \operatorname{div}^2\lambda_2^* = 0, \\ \alpha(u^*)s^* - \lambda_1^* = 0, \quad s^* \in \partial|v^*|, \\ \beta(u^*)p^* - \lambda_2^* = 0, \quad p^* \in \partial|w^*|, \\ \nabla u^* - v^* = 0, \quad \nabla^2 u^* - w^* = 0, \end{cases}$$

for almost every point in  $\Omega$ . This implies that the generated limit point satisfies the first-order optimality conditions (3.9). One can see that the proof of this theorem started with an arbitrary extreme point  $(\bar{u}, \bar{v}, \bar{w}, \bar{\lambda}_1, \bar{\lambda}_2)$ , it follows that the specific extreme point  $(\bar{u}, \bar{v}, \bar{w}, \bar{\lambda}_1, \bar{\lambda}_2) = (u^*, v^*, w^*, \lambda_1^*, \lambda_2^*)$  can be considered as the limit of converging subsequence  $\{(u^{k_l}, v^{k_l}, w^{k_l}, \lambda_1^{k_l}, \lambda_2^{k_l})\}_{l \in \mathbb{N}}$ . More precisely, since  $e_{k_l}$  tends to zero, then the error sequence  $\{e_k\}_{k \in \mathbb{N}}$  converges to zero correspondingly, which denotes that  $\{(u^{k_l}, v^{k_l}, w^{k_l}, \lambda_1^{k_l}, \lambda_2^{k_l})\}$  converges to  $(u^*, v^*, w^*, \lambda_1^*, \lambda_2^*)$  almost everywhere in  $\Omega$  and satisfies the optimality conditions (3.9). Hence, this completes the proof.  $\square$

REMARK 3.2. Obviously, it is necessary to guarantee  $\Delta_1 \geq 0$  and  $\Delta_2 \geq 0$  in the proof of Theorem 3.1. Although the lower bounds of  $\Delta_1$  and  $\Delta_2$  are difficult to

be found, we can indicate the rationality of our assumption by numerical experiment with some case. Fig. 3 presents the behavior of  $\Delta_1$  and  $\Delta_2$  versus iteration numbers on different test images in Fig. 4, where  $\Delta_1 \geq 0$  and  $\Delta_2 \geq 0$  hold for all iterations.

**4. Experimental results.** In this section, comprehensive experiments consisting of three parts-image denoising, image deblurring and image inpainting are implemented to verify the efficiency and superiority of our proposed spatially adapted variational model (called SA-TV-TV<sup>2</sup>). All numerical experiments are performed utilizing Matlab R2016a on a machine with 3.40GHz Intel(R) Core(TM) i7-6700 CPU and 32GB RAM.

In our work, the popular peak signal-to-noise ratio (PSNR) and structural similarity (SSIM) indexes [46] are adopted to quantitatively evaluate the imaging performance under different image degradation conditions. In general, the PSNR is defined as

$$(4.1) \quad \text{PSNR}(u_0, u) = 10 \log \frac{255^2}{\text{MSE}},$$

and the SSIM is

$$(4.2) \quad \text{SSIM}(u_0, u) = \frac{(2\mu_{u_0}\mu_u + c_1)(2\sigma_{u_0u} + c_2)}{(\mu_{u_0}^2 + \mu_u^2 + c_1)(\sigma_{u_0}^2 + \sigma_u^2 + c_2)},$$

where  $u_0$  denotes the clear image,  $u$  represents the recovery image, MSE indicates the mean square error of  $u_0$  and  $u$ .  $\mu_{u_0}$  and  $\mu_u$ , respectively, express the local mean values of images  $u_0$  and  $u$ ,  $\sigma_{u_0}$  and  $\sigma_u$  signify the respective standard deviations,  $c_1$  and  $c_2$  are two constants to avoid instability for near-zero denominator values, and  $\sigma_{u_0u}$  is the covariance value between images  $u_0$  and  $u$ . Theoretically, higher PSNR and SSIM values normally denote better performance in image reconstruction.

In particular, the variation of the residuals as well as the relative errors and energy will give us important information about the convergence of the iterations. During the iterations, the relative residuals are given by

$$(4.3) \quad (R_1^k, R_2^k) = \frac{1}{|\Omega|} (\|v^k - \nabla u^k\|_1, \|w^k - \nabla^2 u^k\|_1).$$

where  $\|\cdot\|_1$  is the  $L^1$  norm on  $\Omega$  and  $|\Omega|$  is the area of domain. To check the convergence of the iteration process, we also check the relative errors of Lagrange multipliers

$$(4.4) \quad (L_1^k, L_2^k) = \left( \frac{\|\lambda_1^k - \lambda_1^{k-1}\|_1}{\|\lambda_1^{k-1}\|_1}, \frac{\|\lambda_2^k - \lambda_2^{k-1}\|_1}{\|\lambda_2^{k-1}\|_1} \right)$$

and the relative error in  $u^k$

$$(4.5) \quad R(u^k) = \frac{\|u^k - u^{k-1}\|_1}{\|u^{k-1}\|_1}.$$

In addition, the numerical energy is calculated as

$$(4.6) \quad E(u^k) = \int_{\Omega} \alpha(u^k) |\nabla u^k| dx + \int_{\Omega} \beta(u^k) |\nabla^2 u^k| dx + \frac{1}{2\lambda} \int_{\Omega} (u^k - f)^2 dx.$$

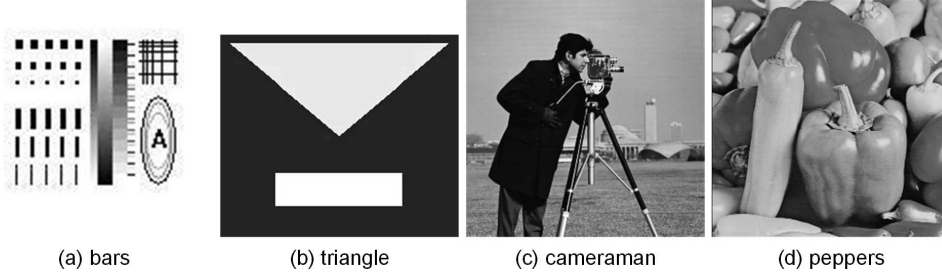


FIG. 4. Test images. From left to right: (a) bars( $128 \times 128$ ), (b) triangle( $254 \times 214$ ), (c) cameraman( $256 \times 256$ ), (d) peppers( $256 \times 256$ ), respectively.

TABLE 1

The tunable parameters of comparative image reconstruction methods. Here,  $\lambda^0$  indicates the initial value of  $\lambda$ , which is dynamically updated for the SATV model.

Methods	Model parameters			Algorithm parameters			
Euler's elastica [44]	$\eta$	$a$	$b$	$r_1$	$r_2$	—	$r_4$
MC [53]	$\lambda$	—	—	$r_1$	$r_2$	$r_3$	$r_4$
TV-TV <sup>2</sup> [38]	—	$\alpha$	$\beta$	$r_1$	$r_2$	—	—
TGV [8]	$\lambda$	$\alpha_0$	$\alpha_1$	$r_1$	$r_2$	—	—
SATV [18]	$\lambda^0$	—	—	$\omega$	$\zeta$	—	—
SA-TV-TV <sup>2</sup>	$\lambda$	—	—	$r_1$	$r_2$	—	—

**4.1. Numerical discretization.** Without loss of generality, our image will be 2-dimensional matrices of size  $M \times N$ . In the discrete setting, we let  $u(i, j)$  be an element of Euclidean space  $\mathbb{R}^{M \times N}$  on the grid  $\Omega_{M,N} = \{(i, j) : 0 \leq i \leq M-1, 0 \leq j \leq N-1\}$ . For an image  $u$ , we define the periodic partial derivatives with the spatial mesh size  $h$  as follows

$$\begin{aligned}\nabla_x^+ u(i, j) &= (u(i+1, j) - u(i, j))/h, \\ \nabla_y^+ u(i, j) &= (u(i, j+1) - u(i, j))/h, \\ \nabla_x^- u(i, j) &= (u(i, j) - u(i-1, j))/h, \\ \nabla_y^- u(i, j) &= (u(i, j) - u(i, j-1))/h.\end{aligned}$$

Therefore, the discrete gradient operator  $\nabla : \mathbb{R}^{M \times N} \rightarrow (\mathbb{R}^{M \times N})^2$  is defined as

$$\nabla u(i, j) = (\nabla_x^+ u(i, j), \nabla_y^+ u(i, j)),$$

and the discrete divergence operator  $\text{div} : (\mathbb{R}^{M \times N})^2 \rightarrow \mathbb{R}^{M \times N}$  for  $p = (p_1, p_2) \in (\mathbb{R}^{M \times N})^2$  is defined by

$$\text{div} p(i, j) = \nabla_x^- p_1(i, j) + \nabla_y^- p_2(i, j).$$

Note that the regularizer of our proposed model is not homogeneous in  $u$  since it is obtained by the level set of an image surface, which is differentiated from some classical image reconstruction models, for instance, the ROF model [41] and high order variational models [2, 4, 33]. Therefore, similar to the mean curvature regularization, the choice of spatial mesh size  $h$  turns into an important issue when discretize the derivatives to achieve excellent reconstruction performance [53].

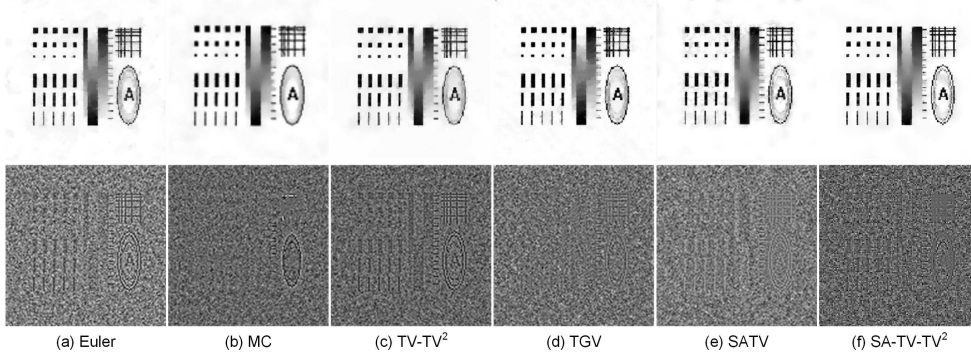


FIG. 5. Denoising results of “bars” (top) and their residual images (bottom) by different methods. The parameters are set as (a) Euler’s elastica:  $a = 1$ ,  $b = 10$ ,  $\eta = 10^2$ ,  $r_1 = 1$ ,  $r_2 = 2 \cdot 10^2$  and  $r_4 = 5 \cdot 10^2$ ; (b) MC:  $r_1 = 20$ ,  $r_2 = 20$ ,  $r_3 = 10^4$ ,  $r_4 = 10^5$  and  $\lambda = 1.5 \cdot 10^3$ ; (c) TV-TV<sup>2</sup>:  $\alpha = 10$ ,  $\beta = 5$ ,  $r_1 = 1$  and  $r_2 = 5$ ; (d) TGV:  $\alpha_0 = 1.5$ ,  $\alpha_1 = 1.0$ ,  $r_1 = 10$ ,  $r_2 = 50$  and  $\lambda = 4$ ; (e) SATV:  $\omega = 11$ ,  $\zeta = 2$  and  $\lambda^0 = 2.0$ ; (f) SA-TV-TV<sup>2</sup>:  $r_1 = 0.1$ ,  $r_2 = 0.5$  and  $\lambda = 160$ .

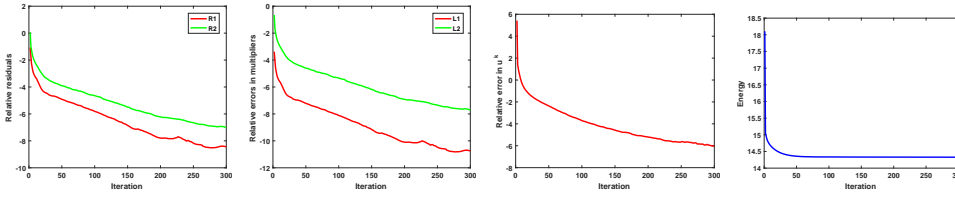


FIG. 6. Evaluations of “bars” by SA-TV-TV<sup>2</sup> method. From left to right: Relative residuals (4.3), relative errors in multipliers (4.4), relative errors in  $u^k$  (4.5) and numerical energy (4.6), respectively.

**4.2. Parameters discussing.** In all experiments, we set the parameters  $\mu = 0$ ,  $\gamma = 0$  and  $\tau = 0$ , which are required for convergence analysis. Since our models are derived on image surface, the spatial mesh size  $h$  influences the reconstruction performance to a certain extent. It is well known that an image is defined on a finite number of grid points such that small spatial mesh size will result in residual noises and large spatial mesh size will lead to the over-smoothed performance. We choose  $h = 5$  throughout the experiments for the best balance between the smoothness and fine details. General speaking, the penalty parameters of  $r_1$  and  $r_2$  control the convergent speed and stability of Algorithm 1. Note that large values of  $r_1$  and  $r_2$  reduce the algorithm’s efficiency and reconstructed image quality, conversely, choosing small values of  $r_1$  and  $r_2$  can obtain extremely fast convergent results but is unstable w.r.t. different test images. It is crucial to select appropriate penalty parameters  $r_1$  and  $r_2$  for balancing both algorithm’s efficiency and stability. The positive constant  $\lambda$  affects the balance between the data-fidelity and regularization terms, which should be selected according to the structures of image and different noise-levels.

We compare the proposed model with the most relevant methods including the Euler’s elastica model (Euler) [44], mean curvature (MC) [53], hybrid first and second order model (TV-TV<sup>2</sup>) [38], the second order total generalized variation model (TGV) [8] and the spatially adapted TV method (SATV) [18]. The tunable parameters of all comparative algorithms are listed in Table 1. As shown, the number of model parameter in our model is smaller than or equal to other comparative methods, which

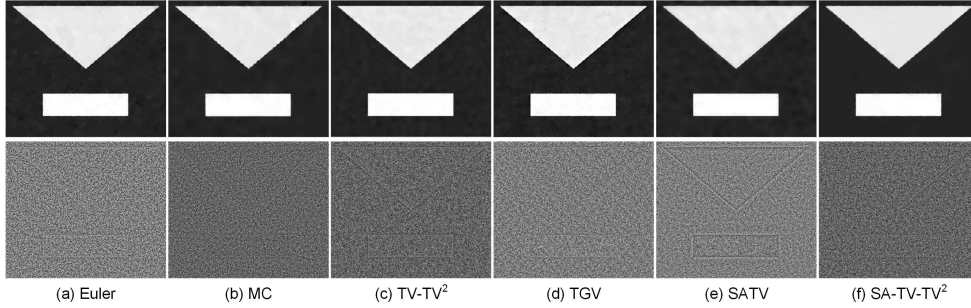


FIG. 7. Denoising results of “triangle” (top) and their residual images (bottom) by different methods. The parameters are set as (a) Euler’s elastica:  $a = 1$ ,  $b = 10$ ,  $\eta = 10^2$ ,  $r_1 = 1$ ,  $r_2 = 2 \cdot 10^2$  and  $r_4 = 5 \cdot 10^2$ ; (b) MC:  $r_1 = 20$ ,  $r_2 = 20$ ,  $r_3 = 10^5$ ,  $r_4 = 10^5$  and  $\lambda = 1.5 \cdot 10^3$ ; (c) TV-TV<sup>2</sup>:  $\alpha = 10$ ,  $\beta = 5$ ,  $r_1 = 1$  and  $r_2 = 5$ ; (d) TGV:  $\alpha_0 = 1.5$ ,  $\alpha_1 = 1.0$ ,  $r_1 = 10$ ,  $r_2 = 50$  and  $\lambda = 4$ ; (e) SATV:  $\omega = 11$ ,  $\zeta = 2$  and  $\lambda^0 = 2.0$ ; (f) SA-TV-TV<sup>2</sup>:  $r_1 = 0.1$ ,  $r_2 = 0.5$  and  $\lambda = 160$ .

TABLE 2

PSNR comparisons of various image denoising methods on test images for restoring noisy images corrupted by Gaussian noise with different standard deviation  $\sigma$ .

Methods	bars	triangle	cameraman	peppers
Euler’s elastica [44]	24.83	32.67	27.85	28.26
MC [53]	26.35	33.65	28.40	29.57
TV-TV <sup>2</sup> [38]	25.42	33.06	27.81	28.50
TGV [8]	25.90	33.41	28.38	29.17
SATV [18]	25.64	32.25	28.28	29.43
SA-TV-TV <sup>2</sup>	<b>27.08</b>	<b>34.30</b>	<b>29.15</b>	<b>30.28</b>

greatly eases the difficulty in selecting parameters. Simultaneously, our model also has fewer algorithm parameters than other high order models including the Euler’s elastica, MC, TV-TV<sup>2</sup> and TGV method, which means fewer subproblems are contained in each iteration and may achieve better computational efficiency. The specific values of parameters for all comparative algorithms are provided in each experiment.

**4.3. Experiments on denoising.** We first illustrate the efficiency and superiority of the proposed method via various examples in image denoising. We choose four grayscale images in Fig. 4 and compare with the aforementioned denoising methods. The synthetic images “bars” and “triangle” are degraded by Gaussian noise with zero mean and the standard deviation 30, while the real images “cameraman” and “peppers” are degraded by Gaussian noise with zero mean and the standard deviation 20. The iteration terminated parameters  $T_{\max} = 300$  and  $\epsilon = 2 \times 10^{-3}$  are exploited for all comparative algorithms throughout this numerical experiment. According to different noise levels, the experience-dependent parameters for our model are set as  $r_1 = 0.1$ ,  $r_2 = 0.5$ ,  $\lambda = 160$  for  $\sigma = 30$  and  $r_1 = 1$ ,  $r_2 = 2$ ,  $\lambda = 100$  for  $\sigma = 20$  in the denoising performances respectively.

**4.3.1. Comparison results.** The denoising results and the residual images  $f - u$  of the synthetic images are visually exhibited in Fig. 5 and Fig. 7, while the denoising results and the selected local magnification views of the real images are shown in Fig. 9 and Fig. 11. In general, all methods can efficiently eliminate the noise, and some methods can well preserve the image structures and features such as MC and SA-TV-TV<sup>2</sup> model. From the magnified images in Fig. 9 and Fig. 11, the TV-TV<sup>2</sup> model tends to obtain over-smooth recovery results resulting in some important

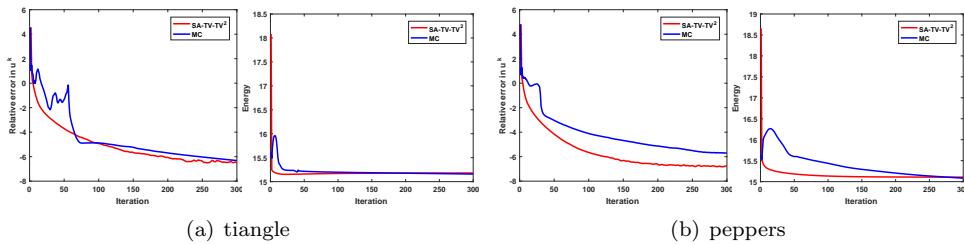


FIG. 8. Compared evaluations of “triangle” and “peppers” by MC and SA-TV-TV<sup>2</sup> methods in terms of relative errors (4.5) and numerical energy (4.6).

TABLE 3

SSIM comparisons of various image denoising methods on test images for restoring noisy images corrupted by Gaussian noise with different standard deviation  $\sigma$ .

Methods	bars	triangle	cameraman	peppers
Euler’s elastica [44]	0.9232	0.9383	0.8138	0.8426
MC [53]	0.9453	0.9663	0.8203	0.8628
TV-TV <sup>2</sup> [38]	0.9308	0.9561	0.8187	0.8571
TGV [8]	0.9380	0.9358	0.8157	0.8474
SATV [18]	0.9354	0.9517	0.8229	0.8613
SA-TV-TV <sup>2</sup>	<b>0.9576</b>	<b>0.9734</b>	<b>0.8314</b>	<b>0.8784</b>

image details and textures loss. The restored images of the Euler’s elastica and TGV method are not as smooth as others in the homogeneous regions. Although the SATV method can achieve almost satisfactory visual results owing to the spatially adapted regularization parameter, it still suffers from some unnatural staircase-like artifacts in the large homogeneous regions such as the black region in Fig. 7. On the other hand, Fig. 5 and Fig. 7 show that the residual images obtained by the Euler’s elastica, TV-TV<sup>2</sup> and SATV method contain much image details, while there is almost no signal information inside the residual images  $f - u$  by MC and our method. Obviously, the contrast preserving methods can help to produce better reconstruction results, which is further demonstrated by the PSNR and SSIM in Tables 2 and 3. Although both MC and our method can preserve image contrasts, the higher PSNR and SSIM are always achieved by our SA-TV-TV<sup>2</sup> as the parameters of our algorithm are fewer than MC model and are easy to select.

We also track the decay of relative residuals (4.3), the relative errors in multipliers (4.4), the relative errors in  $u^k$  (4.5) and the numerical energy (4.6), which are displayed with *log-scale* in Fig. 6 and Fig. 10. The plots demonstrate the convergence of the iterative process and show that the process leads to some saddle points of the constrained minimization problem. Fig. 8 records the curves of the relative error in  $u^k$  and numerical energy decay for the image “triangle” and “peppers” in *log-scale* by the MC and SA-TV-TV<sup>2</sup> model. The plots reveal that the numerical convergence of our SA-TV-TV<sup>2</sup> model is more stable than the MC model. Moreover, the numerical energies obtained by the SA-TV-TV<sup>2</sup> model are close to the ones obtained by the MC model when both algorithms converge.

Besides, we present the CPU time of each method in Table 4, where SA-TV-TV<sup>2</sup> method is faster than other methods except for the Euler’s elastica model. The convergence curves in Fig. 12 of “triangle” and “peppers” also confirm that the Euler’s elastica method converges fastest, and our proposal converges faster than others within the same relative error  $2 \times 10^{-3}$ . Although our model is somehow slower than the

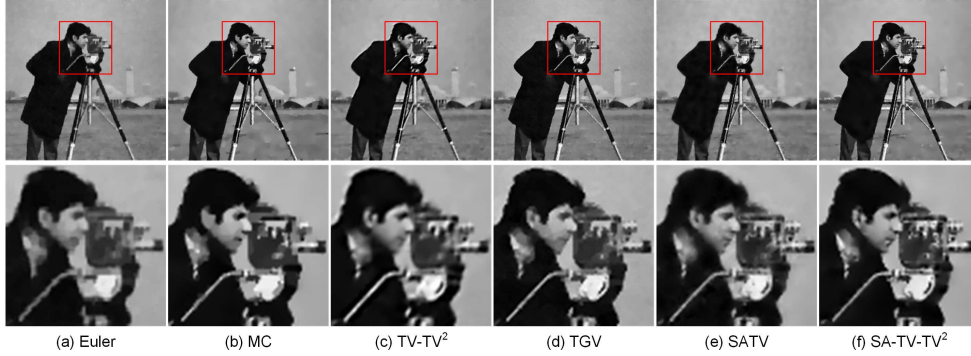


FIG. 9. Denoising results of “cameraman” (top) and their local magnification views (bottom) by different methods. The parameters are set as (a) Euler’s elastica:  $a = 1$ ,  $b = 10$ ,  $\eta = 2 \cdot 10^2$ ,  $r_1 = 1$ ,  $r_2 = 2 \cdot 10^2$  and  $r_4 = 5 \cdot 10^2$ ; (b) MC:  $r_1 = 40$ ,  $r_2 = 40$ ,  $r_3 = 10^5$ ,  $r_4 = 1.5 \cdot 10^5$  and  $\lambda = 10^2$ ; (c) TV-TV<sup>2</sup>:  $\alpha = 5$ ,  $\beta = 10$ ,  $r_1 = 10$  and  $r_2 = 50$ ; (d) TGV:  $\alpha_0 = 1.5$ ,  $\alpha_1 = 1.0$ ,  $r_1 = 10$ ,  $r_2 = 50$  and  $\lambda = 10$ ; (e) SATV:  $\omega = 11$ ,  $\zeta = 2$  and  $\lambda^0 = 2.5$ ; (f) SA-TV-TV<sup>2</sup>:  $r_1 = 1$ ,  $r_2 = 2$  and  $\lambda = 100$ .

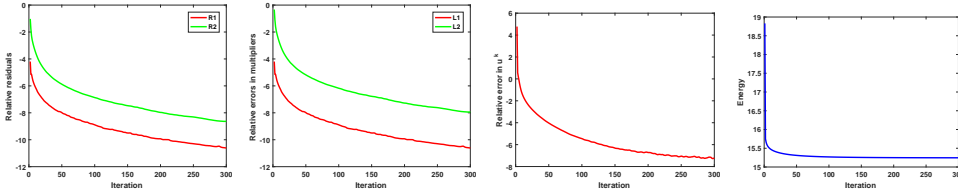


FIG. 10. Evaluations of “cameraman” by the SA-TV-TV<sup>2</sup> method. From left to right: Relative residuals (4.3), relative errors in multipliers (4.4), relative errors in  $u^k$  (4.5) and numerical energy (4.6), respectively.

Euler’s elastica model, we always obtain better recovery results, around 2dB higher. Compared to the MC and SATV method, much CPU time is saved by our SA-TV-TV<sup>2</sup> model without loss of recovery quality. The reason is that our algorithm contains less subproblems in each iteration and can terminate using relative errors, while MC and SATV method usually converge using the maximum iteration number. The above evaluations indicate that our method can produce better image denoising results with high computational efficiency.

**4.3.2. Spatially varying parameters.** The superior results benefits from the spatially adapted regularization parameter  $\alpha(u)$  and  $\beta(u)$ . Fig. 13 and Fig. 14 show that the final values of  $\alpha(u)$  and  $\beta(u)$  are accord with our assumption, i.e., varying with image gradients in an opposite way. More especially, the model adaptively chooses small values of  $\alpha(u)$  and large values of  $\beta(u)$  in the homogeneous regions to remove the noises as well as avoid staircase effect. On the other hand, large values of  $\alpha(u)$  and small values of  $\beta(u)$  are selected in textural regions to allow jumps and enhance edges. Thanks to the non-loss of contrast property, our SA-TV-TV<sup>2</sup> model can well balance the performance of noise removal and feature preservation, and achieve satisfactory recovery results.

**4.3.3. Impact of parameters.** In order to discuss the impact of  $r_1$ ,  $r_2$  and  $\lambda$  in Algorithm 1, we use the images “bars” and “cameraman” as examples to illustrate the recovery qualities with respect to different parameters. First, we vary the pa-

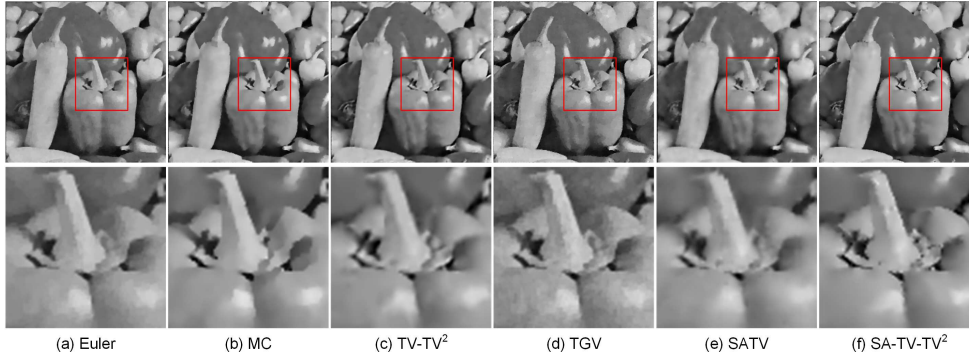


FIG. 11. Denoising results of “peppers” (top) and their local magnification views (bottom) by different methods. The parameters are set as (a) Euler’s elastica:  $a = 1$ ,  $b = 10$ ,  $\eta = 2 \cdot 10^2$ ,  $r_1 = 1$ ,  $r_2 = 2 \cdot 10^2$  and  $r_4 = 5 \cdot 10^2$ ; (b) MC:  $r_1 = 40$ ,  $r_2 = 40$ ,  $r_3 = 10^5$ ,  $r_4 = 10^5$  and  $\lambda = 10^2$ ; (c) TV-TV<sup>2</sup>:  $\alpha = 5$ ,  $\beta = 10$ ,  $r_1 = 10$  and  $r_2 = 50$ ; (d) TGV:  $\alpha_0 = 1.5$ ,  $\alpha_1 = 1.0$ ,  $r_1 = 10$ ,  $r_2 = 50$  and  $\lambda = 10$ ; (e) SATV:  $\omega = 11$ ,  $\zeta = 2$  and  $\lambda^0 = 2.5$ ; (f) SA-TV-TV<sup>2</sup>:  $r_1 = 1$ ,  $r_2 = 2$  and  $\lambda = 100$ .

TABLE 4

Time comparisons of various image denoising methods on test images for restoring noisy images corrupted by Gaussian noise with different standard deviation  $\sigma$ .

Methods	bars	triangle	cameraman	peppers
Euler’s elastica [44]	<b>2.48</b>	<b>7.52</b>	<b>8.69</b>	<b>8.51</b>
MC [53]	21.19	65.78	68.59	68.08
TV-TV <sup>2</sup> [38]	7.94	21.06	22.58	22.15
TGV [8]	10.09	30.18	31.98	31.32
SATV [18]	24.54	98.85	105.93	103.14
SA-TV-TV <sup>2</sup>	5.67	15.41	16.42	16.25

parameters  $(r_1, r_2) \in \{r_1^0 \times 2^{-l_1}, r_1^0 \times 2^{-l_1+1}, \dots, r_1^0 \times 2^{l_1-1}, r_1^0 \times 2^{l_1}\} \times \{r_2^0 \times 2^{-l_2}, r_2^0 \times 2^{-l_2+1}, \dots, r_2^0 \times 2^{l_2-1}, r_2^0 \times 2^{l_2}\}$  with  $r_1^0 = 16$ ,  $r_2^0 = 32$  and  $l_1 = l_2 = 12$ . Then, we select  $\lambda \in \{80, 160, 320\}$  for the image “bars” and  $\lambda \in \{40, 100, 250\}$  for the image “cameraman”. As shown in Fig. 15 and Fig. 16, for fixed  $\lambda$ , there are relative large intervals for  $r_1$  and  $r_2$  to generate good restoration results. Furthermore, we also show the best recovery results among various combinations of  $r_1, r_2$  for each  $\lambda = 80, 160, 320$  of the image “bar” in Fig. 15 and  $\lambda = 40, 100, 250$  of the image “cameraman” in Fig. 16. It can be observed that small  $\lambda$  leads to non-smooth recovery results with some noise remaining, while large  $\lambda$  results in over-smooth recovery results with some details missing. Hence, the choice of  $\lambda$  is related to the noise level contained in the images such that the larger the noises are, the larger  $\lambda$  should be.

**4.4. Experiments on deblurring.** In this subsection, we implement the image deblurring experiments under different degradations to illustrate the efficiency of our proposed method. The corresponding deblurring model can be formalized as

$$(4.7) \quad \min_u \int_{\Omega} \alpha(u) |\nabla u| dx + \int_{\Omega} \beta(u) |\nabla^2 u| dx + \frac{1}{2\lambda} \int_{\Omega} |Ku - f|^2 dx,$$

where the operator  $K$  denotes blur kernel.

The clear image “house” is corrupted by Gaussian blur kernel (fspecial(‘gaussian’, [7 7], 2)) and Gaussian noise of zero mean and standard deviation 5 in Fig. 17(a), and the original image “tomato” is degraded by the average blur kernel (fspecial(‘average’, [7 7])), followed by adding Gaussian noise of zero mean with standard deviation 10

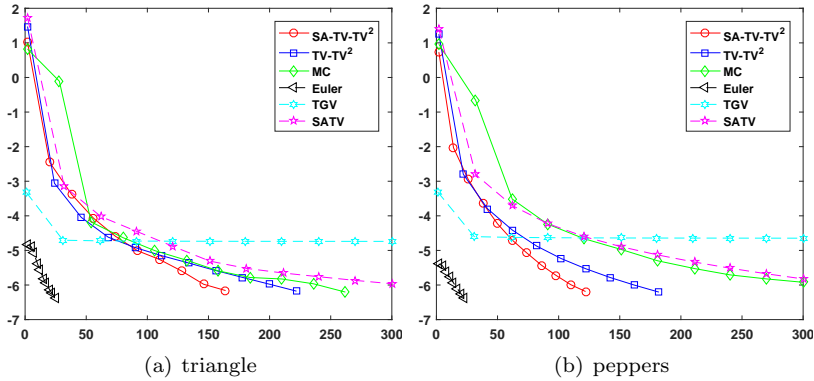


FIG. 12. Convergence curves of “triangle” and “peppers” by different methods.

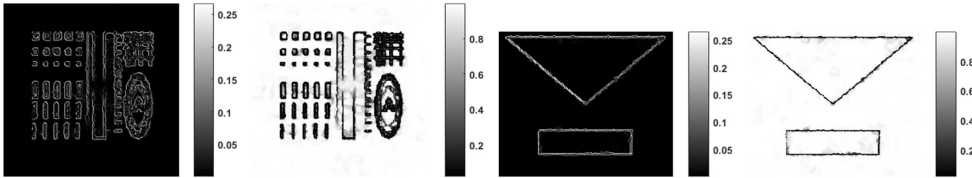


FIG. 13. The spatially adaptive values of synthetic images in SA-TV-TV<sup>2</sup> method. From left to right:  $\alpha(u)$  of “bars”,  $\beta(u)$  of “bars”,  $\alpha(u)$  of “triangle”,  $\beta(u)$  of “triangle”, respectively.

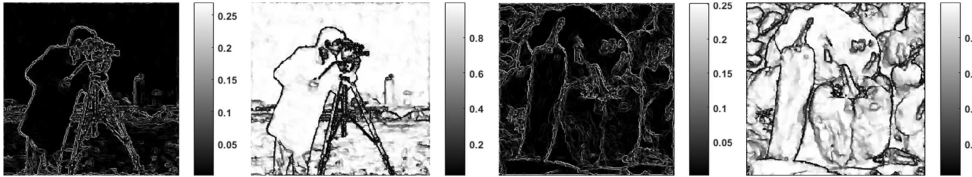


FIG. 14. The spatially adaptive values of real images in SA-TV-TV<sup>2</sup> method. From left to right:  $\alpha(u)$  of “cameraman”,  $\beta(u)$  of “cameraman”,  $\alpha(u)$  of “peppers”,  $\beta(u)$  of “peppers”, respectively.

in Fig. 18(a). We set  $r_1 = r_2 = 4$ ,  $\lambda = 5$  and  $r_1 = r_2 = 0.2$ ,  $\lambda = 15$  for “house” and “tomato”, respectively. A series of experiments are conducted by comparing the SA-TV-TV<sup>2</sup> and TV-TV<sup>2</sup> method with different combinations of regularization parameters, i.e.  $\beta = 0$ ,  $\alpha = 0$  and  $\alpha \neq 0, \beta \neq 0$ . The image deblurring results and their local magnification views of the SA-TV-TV<sup>2</sup> and TV-TV<sup>2</sup> method are displayed in Fig. 17 and Fig. 18, while the quantitative results are detailed in Table 5 and 6.

We can see that both the recovery images of SA-TV-TV<sup>2</sup> and TV-TV<sup>2</sup> model suffer from serious staircasing artifacts in the case of  $\beta = 0$ , the main reason behind which is that the first order TV regularizer favors piecewise constant solutions. On the other hand, when  $\alpha = 0$ , the results tend to be over-smoothed. It is worthy to mention that, compared to the TV-TV<sup>2</sup> model, our SA-TV-TV<sup>2</sup> model can well recover the sharp edges in restoration results, see the magnified view of the images “house” and “tomato”. The visual comparisons are further confirmed by the quantitative results in terms of PSNR and SSIM as explored in Tables 5 and 6, where the best PSNR and SSIM are always obtained by the SA-TV-TV<sup>2</sup> model with non-zero spatially varying

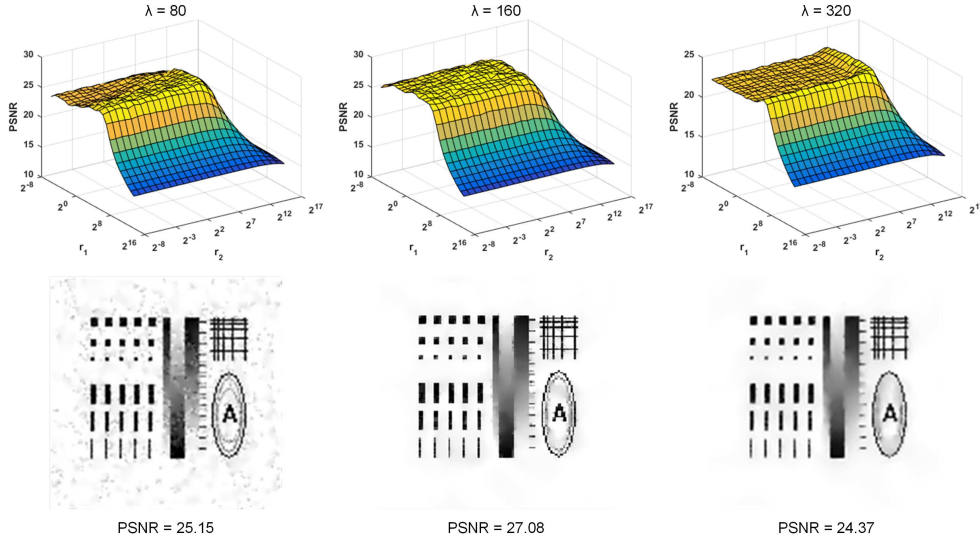


FIG. 15. PSNRs of “bars” by different penalty factors with fixed regularized parameters in SA-TV-TV<sup>2</sup> method. From left to right: the results of  $\lambda = 80$ ,  $\lambda = 160$  and  $\lambda = 320$ , respectively.

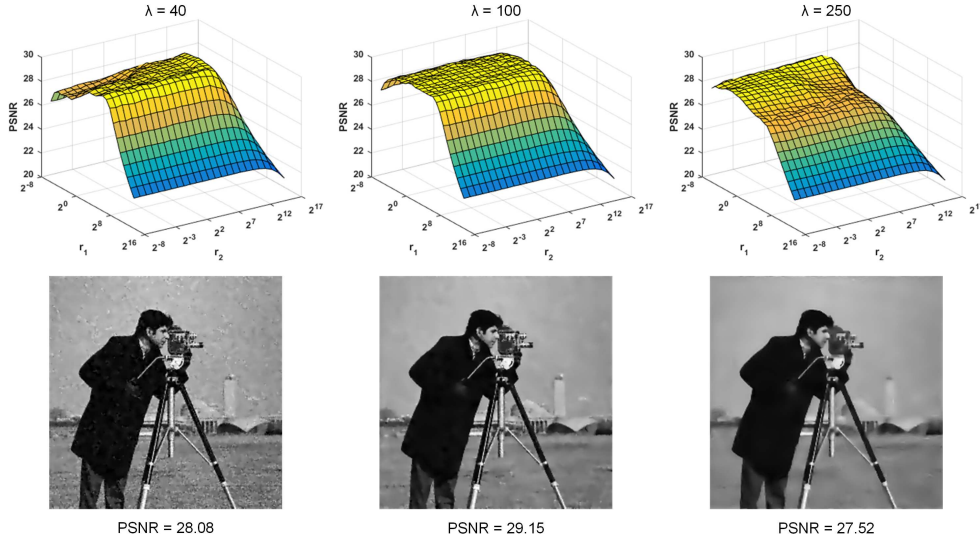


FIG. 16. PSNRs of “cameraman” by different penalty factors with fixed regularized parameters in SA-TV-TV<sup>2</sup> method. From left to right: the results of  $\lambda = 40$ ,  $\lambda = 100$  and  $\lambda = 250$ , respectively.

$\alpha$  and  $\beta$ .

**4.5. Experiments on inpainting.** Finally, we demonstrate some examples of our SA-TV-TV<sup>2</sup> method for image inpainting problems. In general, the task of image inpainting is to reconstruct a missing part of an image using information from the intact part. The missing part of the image is called the inpainting domain and is denoted by  $D \subseteq \Omega$ . Image inpainting has attracted extensive attention in the fields of image processing and computer vision, such as TV inpainting [22], curvature driven

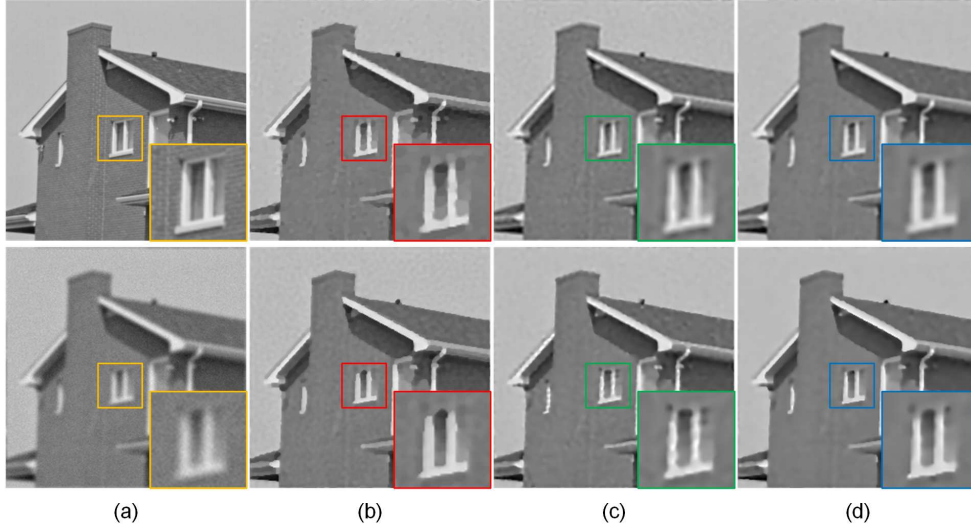


FIG. 17. Deblurring comparisons of different parameters in  $TV-TV^2$  and  $SA-TV-TV^2$  methods on test image “house”. From left to right: (a) clear image and degraded image, (b) recovery images by  $TV-TV^2$  method with  $\alpha = 0.4, \beta = 0$  and  $SA-TV-TV^2$  method with  $\beta = 0$ , (c) recovery images by  $TV-TV^2$  method with  $\alpha = 0, \beta = 0.4$  and  $SA-TV-TV^2$  method with  $\alpha = 0$ , (d) recovery images by  $TV-TV^2$  method with  $\alpha = 0.4, \beta = 0.4$  and  $SA-TV-TV^2$  method, respectively.

TABLE 5

Evaluated comparisons of different parameters in  $TV-TV^2$  and  $SA-TV-TV^2$  methods on test image “house” for restoring degraded image corrupted by Gaussian blur kernel with Gaussian noise of standard deviation  $\sigma = 5$ .

$TV-TV^2$	$\alpha = 0.4, \beta = 0$	$\alpha = 0, \beta = 0.4$	$\alpha = 0.4, \beta = 0.4$
PSNR	29.71	29.47	29.85
SSIM	0.8121	0.8027	0.8168
$SA-TV-TV^2$	$\alpha = \alpha(u), \beta = 0$	$\alpha = 0, \beta = \beta(u)$	$\alpha = \alpha(u), \beta = \beta(u)$
PSNR	29.25	29.92	<b>30.35</b>
SSIM	0.7992	0.8193	<b>0.8236</b>

diffusion inpainting [13], Mumford-Shah based inpainting [21] and Euler’s elastica inpainting [44]. The spatially varying first and second order regularized inpainting model is given as follows

$$\min_u \int_{\Omega} \alpha(u) |\nabla u| dx + \int_{\Omega} \beta(u) |\nabla^2 u| dx + \frac{1}{2\lambda} \int_{\Omega \setminus D} |u - f|^2 dx.$$

Three auxiliary variables are introduced to rewrite the above minimization problem into a constrained one:

$$(4.8) \quad \min_{\tilde{u}, v, w} \int_{\Omega} \alpha(u) |v| dx + \int_{\Omega} \beta(u) |w| dx + \frac{1}{2\lambda} \int_{\Omega \setminus D} (z - f)^2 dx$$

s.t.  $z = u, v = \nabla u, w = \nabla^2 u.$

More details for dealing with the constraint optimization problem (4.8) can be referred to [39].

In Fig. 19, we present two convincing examples of image inpainting by our method. We can observe that the reconstructed images, i.e., Fig. 19 (a2) and (b2),

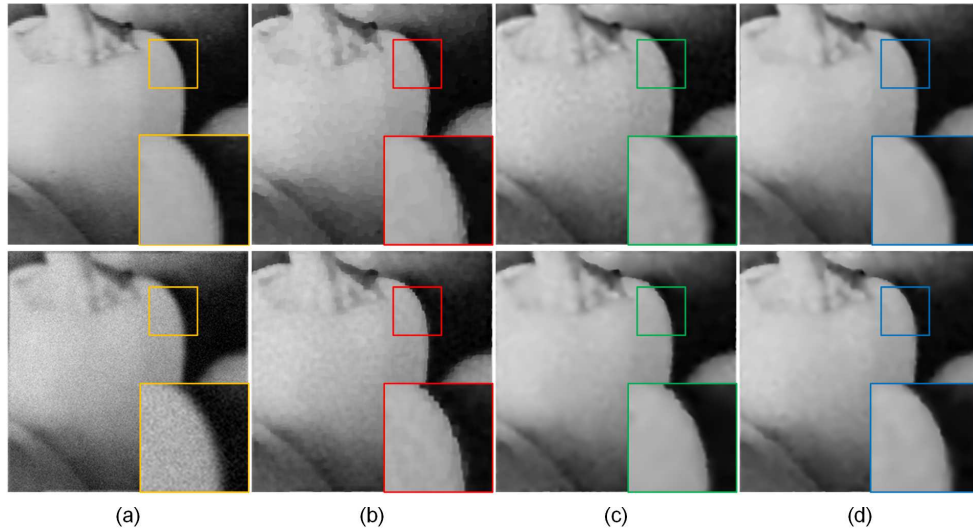


FIG. 18. Deblurring comparisons of different parameters in  $TV-TV^2$  and  $SA-TV-TV^2$  methods on test image “tomato”. From left to right: (a) clear image and degraded image, (b) recovery images by  $TV-TV^2$  method with  $\alpha = 1.5, \beta = 0$  and  $SA-TV-TV^2$  method with  $\beta = 0$ , (c) recovery images by  $TV-TV^2$  method with  $\alpha = 0, \beta = 1.5$  and  $SA-TV-TV^2$  method with  $\alpha = 0$ , (d) recovery images by  $TV-TV^2$  method with  $\alpha = 1.5, \beta = 1.5$  and  $SA-TV-TV^2$  method, respectively.

TABLE 6

Evaluated comparisons of different parameters in  $TV-TV^2$  and  $SA-TV-TV^2$  methods on test image “tomato” for restoring degraded image corrupted by Average blur kernel with Gaussian noise of standard deviation  $\sigma = 10$ .

$TV-TV^2$	$\alpha = 1.5, \beta = 0$	$\alpha = 0, \beta = 1.5$	$\alpha = 1.5, \beta = 1.5$
PSNR	33.30	31.82	32.38
SSIM	0.8746	0.8885	0.9050
$SA-TV-TV^2$	$\alpha = \alpha(u), \beta = 0$	$\alpha = 0, \beta = \beta(u)$	$\alpha = \alpha(u), \beta = \beta(u)$
PSNR	32.58	33.75	<b>34.34</b>
SSIM	0.8704	0.9102	<b>0.9173</b>

are quite natural and extremely similar to the original images. In addition, we compare the  $SA-TV-TV^2$  model,  $TV-TV^2$  model [39] and Euler’s elastica model [44] on a synthetic image in Fig. 20. As shown by Fig. 20 (b) and (f), the TV inpainting model with constant parameter gives nearly piecewise constant result inside the inpainting domain, while the TV model with adaptive parameter also fails to fill such a large gap between the two branches. Actually, the  $TV^2$  model can somehow connect the gap as shown by Fig. 20 (c) and (u), the drawback of which is the boundaries between the two branches are not straight enough, especially Fig. 20 (c). Similar problem happens for Fig. 20 (d) obtained by the  $TV-TV^2$  method and the Euler’s elastica method as shown in Fig. 20 (e). It is clearly shown that our  $SA-TV-TV^2$  model gives the visually best inpainting results, which well recovers the inpainting domain without too much outliers, see Fig. 20 (h).

**5. Conclusion.** Images are commonly composed of multiple objects of different scales, the constant regularization parameters can easily result in remaining noises and losing details in image reconstruction. From this point of view, we proposed a spatially adapted first and second order regularization for image reconstruction,



FIG. 19. Inpainting results of real images by the SA-TV-TV<sup>2</sup> method. The parameters are selected as  $r_1 = 2$ ,  $r_2 = 4$ ,  $r_3 = 0.005$  and  $\lambda = 2$ .

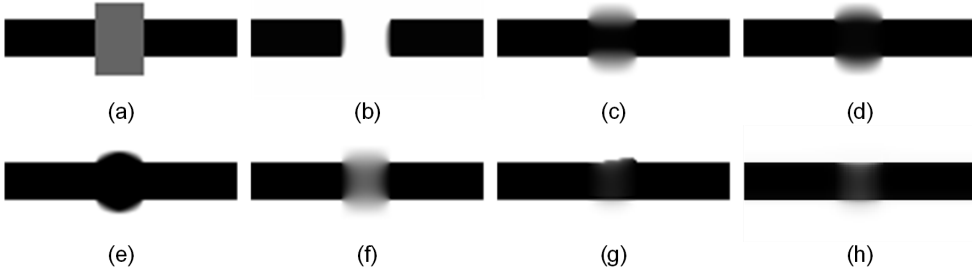


FIG. 20. Inpainting comparisons of different parameters in TV-TV<sup>2</sup>, Euler's elastica and SA-TV-TV<sup>2</sup> methods. From left to right and top to bottom: (a) the degraded image, (b) TV with  $\alpha = 10$ , (c) TV<sup>2</sup> with  $\beta = 5$ , (d) TV-TV<sup>2</sup> with  $\alpha = 10, \beta = 5$ , (e) Euler's elastica model, (f) TV with  $\alpha(u)$  in (2.14), (g) TV<sup>2</sup> with  $\beta(u)$  in (2.14) and (h) SA-TV-TV<sup>2</sup>.

which can not only overcome the staircase artifacts and eliminate the degraded effects, but also have the capacity to preserve image contrast and edges. The minimization problem is effectively solved by the ADMM-based algorithm, where all subproblems can be solved by either FFT or the closed-form solutions. Moreover, we showed the subsequence generated by the ADMM converges to a point satisfying the first-order optimality condition under certain conditions. The numerical experiments on both real and synthetic images have illustrated the efficacious and ascendant performance of our proposed method by comparing with several advanced algorithms. Obviously, the novel regularization scheme can be applied to other image processing problems such as image segmentation, image smoothing, etc. Another possible research direction is to develop an automatic way to select the parameter  $\lambda$  in (2.14), which will further improve its friendliness in real applications.

**Acknowledgment.** The authors would like to thank Prof. Wei Zhu from the University of Alabama for providing us with MATLAB code of [53]. The work is supported by National Natural Science Foundation of China (NSFC 11701418), Major Science and Technology Project of Tianjin 18ZXRHSY00160 and Recruitment Program of Global Young Expert.

#### REFERENCES

- [1] ANDRÉS ALMANSA, COLOMA BALLESTER, VICENT CASELLES, AND GLORIA HARO, *A tv based restoration model with local constraints*, Journal of Scientific Computing, 34 (2008), pp. 209–236.

- [2] EGIL BAE, JUAN SHI, AND XUE-CHENG TAI, *Graph cuts for curvature based image denoising*, IEEE Transactions on Image Processing, 20 (2011), pp. 1199–1210.
- [3] AMIR BECK AND MARC TEBoulLE, *A fast iterative shrinkage-thresholding algorithm for linear inverse problems*, SIAM Journal on Imaging Sciences, 2 (2009), pp. 183–202.
- [4] MAÏTINE BERGOUNIOUX AND LOIC PIFFET, *A second-order model for image denoising*, Set-Valued and Variational Analysis, 18 (2010), pp. 277–306.
- [5] MARCELO BERTALMÍO, VICENT CASELLES, BERNARD ROUGÉ, AND A SOLÉ, *Tv based image restoration with local constraints*, Journal of Scientific Computing, 19 (2003), pp. 95–122.
- [6] JOSÉ M BIUCAS-DIAS AND MÁRIO AT FIGUEIREDO, *A new twist: two-step iterative shrinkage/thresholding algorithms for image restoration*, IEEE Transactions on Image Processing, 16 (2007), pp. 2992–3004.
- [7] KRISTIAN BREDIES, YIQIU DONG, AND MICHAEL HINTERMÜLLER, *Spatially dependent regularization parameter selection in total generalized variation models for image restoration*, International Journal of Computer Mathematics, 90 (2013), pp. 109–123.
- [8] KRISTIAN BREDIES, KARL KUNISCH, AND THOMAS POCK, *Total generalized variation*, SIAM Journal on Imaging Sciences, 3 (2010), pp. 492–526.
- [9] XAVIER BRESSON, SELIM ESEDOĞLU, PIERRE VANDERGHEYNST, JEAN-PHILIPPE THIRAN, AND STANLEY OSHER, *Fast global minimization of the active contour/snake model*, Journal of Mathematical Imaging and vision, 28 (2007), pp. 151–167.
- [10] ANTONIN CHAMBOLLE AND PIERRE-LOUIS LIONS, *Image recovery via total variation minimization and related problems*, Numerische Mathematik, 76 (1997), pp. 167–188.
- [11] TONY CHAN, ANTONIO MARQUINA, AND PEP MULET, *High-order total variation-based image restoration*, SIAM Journal on Scientific Computing, 22 (2000), pp. 503–516.
- [12] TONY F CHAN, SELIM ESEDOĞLU, AND FREDERICK E PARK, *Image decomposition combining staircase reduction and texture extraction*, Journal of Visual Communication and Image Representation, 18 (2007), pp. 464–486.
- [13] TONY F CHAN AND JIANHONG SHEN, *Non-texture inpainting by curvature-driven diffusions*, Journal of Visual Communication and Image Representation, 12 (2001), pp. 436–449.
- [14] YUNMEI CHEN, WILLIAM W HAGER, MARYAM YASHTINI, XIAOJING YE, AND HONGCHAO ZHANG, *Bregman operator splitting with variable stepsize for total variation image reconstruction*, Computational Optimization and Applications, 54 (2013), pp. 317–342.
- [15] C CHUNG, JUAN CARLOS DE LOS REYES, AND CAROLA-BIBIANE SCHÖNLIEB, *Learning optimal spatially-dependent regularization parameters in total variation image restoration*, ArXiv Preprint ArXiv:1603.09155, (2016).
- [16] JUAN CARLOS DE LOS REYES AND CAROLA-BIBIANE SCHÖNLIEB, *Image denoising: Learning the noise model via nonsmooth pde-constrained optimization*, Inverse Problems and Imaging, 7 (2013), pp. 1183–1214.
- [17] LIANG-JIAN DENG, ROLAND GLOWINSKI, AND XUE-CHENG TAI, *A new operator splitting method for the euler elastica model for image smoothing*, SIAM Journal on Imaging Sciences, 12 (2019), pp. 1190–1230.
- [18] YIQIU DONG, MICHAEL HINTERMÜLLER, AND M MONSERRAT RINCON-CAMACHO, *Automated regularization parameter selection in multi-scale total variation models for image restoration*, Journal of Mathematical Imaging and Vision, 40 (2011), pp. 82–104.
- [19] ———, *A multi-scale vectorial  $\ell^1$ -tv framework for color image restoration*, International Journal of Computer Vision, 92 (2011), pp. 296–307.
- [20] MATTHEW ELSEY AND SELIM ESEDOĞLU, *Analogue of the total variation denoising model in the context of geometry processing*, Multiscale Modeling and Simulation, 7 (2009), pp. 1549–1573.
- [21] SELIM ESEDOĞLU AND JIANHONG SHEN, *Digital inpainting based on the mumford-shah-euler image model*, European Journal of Applied Mathematics, 13 (2002), pp. 353–370.
- [22] PASCAL GETREUER, *Total variation inpainting using split bregman*, Image Processing On Line, 2 (2012), pp. 147–157.
- [23] GUY GILBOA, NIR SOCHEN, AND YEHOShUA Y ZEEVI, *Variational denoising of partly textured images by spatially varying constraints*, IEEE Transactions on Image Processing, 15 (2006), pp. 2281–2289.
- [24] WALTER HINTERBERGER AND OTMAR SCHERZER, *Variational methods on the space of functions of bounded hessian for convexification and denoising*, Computing, 76 (2006), pp. 109–133.
- [25] MICHAEL HINTERMÜLLER AND CARLOS N RAUTENBERG, *Optimal selection of the regularization function in a weighted total variation model. part i: Modelling and theory*, Journal of Mathematical Imaging and Vision, 59 (2017), pp. 498–514.
- [26] MICHAEL HINTERMÜLLER, CARLOS N RAUTENBERG, TAO WU, AND ANDREAS LANGER, *Optimal selection of the regularization function in a weighted total variation model. part ii: Algo-*

- rithm, its analysis and numerical tests*, Journal of Mathematical Imaging and Vision, 59 (2017), pp. 515–533.
- [27] MICHAEL HINTERMÜLLER AND M MONSERRAT RINCON-CAMACHO, *Expected absolute value estimators for a spatially adapted regularization parameter choice rule in  $l_1$ -tv-based image restoration*, Inverse Problems, 26 (2010), p. 085005.
- [28] KARL KUNISCH AND THOMAS POCK, *A bilevel optimization approach for parameter learning in variational models*, SIAM Journal on Imaging Sciences, 6 (2013), pp. 938–983.
- [29] ANDREAS LANGER, *Automated parameter selection for total variation minimization in image restoration*, Journal of Mathematical Imaging and Vision, 57 (2017), pp. 239–268.
- [30] SUK-HO LEE AND JIN KEUN SEO, *Noise removal with gauss curvature-driven diffusion*, IEEE Transactions on Image Processing, 14 (2005), pp. 904–909.
- [31] FANG LI, MICHAEL K NG, AND CHAOMIN SHEN, *Multiplicative noise removal with spatially varying regularization parameters*, SIAM Journal on Imaging Sciences, 3 (2010), pp. 1–20.
- [32] HAIYONG LIAO, FANG LI, AND MICHAEL K NG, *Selection of regularization parameter in total variation image restoration*, JOSA A, 26 (2009), pp. 2311–2320.
- [33] RYAN WEN LIU, LIN SHI, CH SIMON, AND DEFENG WANG, *Box-constrained second-order total generalized variation minimization with a combined  $l_1$ ,  $l_2$  data-fidelity term for image reconstruction*, Journal of Electronic Imaging, 24 (2015), p. 033026.
- [34] YAN LIU, JIANHUA MA, YI FAN, AND ZHENGRONG LIANG, *Adaptive-weighted total variation minimization for sparse data toward low-dose x-ray computed tomography image reconstruction*, Physics in Medicine and Biology, 57 (2012), pp. 7923–7956.
- [35] MARIUS LYSAKER, ARVID LUNDERVOLD, AND XUE-CHENG TAI, *Noise removal using fourth-order partial differential equation with applications to medical magnetic resonance images in space and time*, IEEE Transactions on Image Processing, 12 (2003), pp. 1579–1590.
- [36] MARIUS LYSAKER AND XUE-CHENG TAI, *Iterative image restoration combining total variation minimization and a second-order functional*, International Journal of Computer Vision, 66 (2006), pp. 5–18.
- [37] STANLEY OSHER AND RONALD FEDKIW, *Level set methods and dynamic implicit surfaces*, Springer-Verlag, New York, 2002.
- [38] KONSTANTINOS PAPAITSOROS AND CAROLA-BIBIANE SCHÖNLIEB, *A combined first and second order variational approach for image reconstruction*, Journal of Mathematical Imaging and Vision, 48 (2014), pp. 308–338.
- [39] KONSTANTINOS PAPAITSOROS, CAROLA BIBIANE SCHÖNLIEB, AND BATI SENGUL, *Combined first and second order total variation inpainting using split bregman*, Image Processing On Line, 3 (2013), pp. 112–136.
- [40] J. C. DE LOS REYES, C. B. SCHÖNLIEB, AND T. VALKONEN, *Bilevel parameter learning for higher-order total variation regularisation models*, Journal of Mathematical Imaging and Vision, 57 (2017), pp. 1–25.
- [41] LEONID I RUDIN, STANLEY OSHER, AND EMAD FATEMI, *Nonlinear total variation based noise removal algorithms*, Physica D: Nonlinear Phenomena, 60 (1992), pp. 259–268.
- [42] JIANHONG SHEN, SUNG HA KANG, AND TONY F CHAN, *Euler’s elastica and curvature-based inpainting*, SIAM Journal on Applied Mathematics, 63 (2003), pp. 564–592.
- [43] DAVID STRONG AND TONY CHAN, *Edge-preserving and scale-dependent properties of total variation regularization*, Inverse problems, 19 (2003), p. S165.
- [44] XUE-CHENG TAI, JOOYOUNG HAHN, AND GINMO JASON CHUNG, *A fast algorithm for euler’s elastica model using augmented lagrangian method*, SIAM Journal on Imaging Sciences, 4 (2011), pp. 313–344.
- [45] VICTOR A TOPONOGOV, *Differential geometry of curves and surfaces*, Springer, 2006.
- [46] ZHOU WANG, ALAN C BOVIK, HAMID R SHEIKH, AND EERO P SIMONCELLI, *Image quality assessment: from error visibility to structural similarity*, IEEE Transactions on Image Processing, 13 (2004), pp. 600–612.
- [47] YOU-WEI WEN AND RAYMOND H CHAN, *Parameter selection for total-variation-based image restoration using discrepancy principle*, IEEE Transactions on Image Processing, 21 (2012), pp. 1770–1781.
- [48] YOU-WEI WEN, MICHAEL K NG, AND YU-MEI HUANG, *Efficient total variation minimization methods for color image restoration*, IEEE Transactions on Image Processing, 17 (2008), pp. 2081–2088.
- [49] CHUNLIN WU AND XUE-CHENG TAI, *Augmented lagrangian method, dual methods, and split bregman iteration for rof, vectorial tv, and high order models*, SIAM Journal on Imaging Sciences, 3 (2010), pp. 300–339.
- [50] MARYAM YASHTINI AND SUNG HA KANG, *A fast relaxed normal two split method and an effective weighted tv approach for euler’s elastica image inpainting*, SIAM Journal on Imaging

- Sciences, 9 (2016), pp. 1552–1581.
- [51] QIANGQIANG YUAN, LIANGPEI ZHANG, AND HUANFENG SHEN, *Multiframe super-resolution employing a spatially weighted total variation model*, IEEE Transactions on Circuits and Systems for Video Technology, 22 (2012), pp. 379–392.
  - [52] WEI ZHU AND TONY CHAN, *Image denoising using mean curvature of image surface*, SIAM Journal on Imaging Sciences, 5 (2012), pp. 1–32.
  - [53] WEI ZHU, XUE-CHENG TAI, AND TONY CHAN, *Augmented lagrangian method for a mean curvature based image denoising model*, Inverse Problems and Imaging, 7 (2013), pp. 1409–1432.